DEVELOPMENTS IN PHOTOREFRACTIVE TWO-BEAM COUPLING SYSTEMS

by

Valéria B. Damião

B.A., University of Brasília, Brazil, 1990

M.S., University of Colorado, USA, 1995

A thesis submitted to the

Faculty of the Graduate School of the

University of Colorado in partial fulfillment

of the requirements for the degree of

Doctor of Philosophy

Department of Electrical & Computer Engineering

2000

This thesis entitled:
Developments in Photorefractive Two-Beam Coupling Systems
written by Valéria B. Damião
has been approved for the
Department of Electrical & Computer Enginneering

_____
Dr. Dana Z. Anderson

_____
Dr. Kelvin Wagner

Date_____

The final copy of this thesis has been examined by the signatories, and we find that both the content and the form meet acceptable presentation standards fo scholarly work in the above mentioned discipline.

Damião, Valéria B. (Ph.D. Electrical Engineering)

Developments in Photorefractive Two-Beam Coupling Systems.

Thesis directed by Dr. Dana Z. Anderson

Photorefractive systems hold the promise for improving the performance of photonic signal processing applications. This thesis describes several developments pertaining to such systems, in particular to those employing two-beam coupling.

The utility of photorefractive systems is stymied by the lack of a component-oriented technology. Conventionally, an entire optical table, full of mirror mounts and other optical components, is required to build a photorefractive system. To address this shortfall, two-beam coupling modules were designed and fabricated, whose ports were standard multimode fiber optic connectors instead of free-space propagating beams, dispensing with the need for time-consuming alignment and adjustments. These modules employ lenses to couple light into and out of our chosen photorefractive medium, crystalline barium titanate. We demonstrate the utility of the modular concept by implementing an autotuning filter constructed solely by these modules.

For even greater integration of the two-beam coupling units, we present a novel spherical crystal geometry which incorporates the functions of both the lenses and of the photorefractive medium in a single element. While investigating these spherical crystals, we observed internal whispering-gallery mode oscillations. These oscillating patterns adopted simple polygonal shapes depending on the pump entry and crystal-axis angles. We modeled the occurrence conditions of the lowest order

triangle pattern by assuming a single two-beam coupling interaction, using standard plane-wave theory.

Also, as part of a higher-level photonic system, we required a carrier suppressor to remove unwanted correlation between different signal-containing beams. By use of two-beam coupling in the novelty-filter configuration, we obtained more than 70 dB of carrier suppression, to our knowledge, the highest reported in the literature. The use of a simplified, geometrical interpretation of an operator theory for two-beam coupling, which provided the proper choice of parameters needed for perfect suppression, was crucial in obtaining this result.

Finally, the full formalism of the operator theory for two-beam coupling is introduced. This formalism provides the freedom of representing the information to best suit the information-processing problem at hand. A closed-form solution for complex coupling is presented for the case of a single spatial mode interaction, the "2-by-2" case. The already reported solutions for pure-real coupling, corresponding to energy transfer only, and that for pure-imaginary coupling, phase transfer only, are given as special cases of the 2-by-2 complex coupling solution.

A meus queridos pais, pela constante e incansável dedicação.

ACKNOWLEDGMENTS

I gratefully acknowledge the following:

First, Prof. Dana Anderson, for the opportunity to work on a well equipped laboratory and for the financial support (with the exception of the last semester) without which this Ph.D. would not have been possible. I am grateful for the most salient, eye-opening, of his teachings: the essentiality of socio-political and communication skills for a successful career.

Most of all, Bruce Tiemann, my partner and unofficial experimental advisor, for his dedication in teaching me the workings of nature in so many different aspects and for helping me develop a set of laboratory skills of fundamental importance on the work developed in this thesis.

Specially, Vladimir Schkunov and Ben Thompson, for their patience in elucidating numerous theoretical questions, and Prof. Kelvin Wagner for kindly listening and providing academic counseling.

Finally, all colleagues who participated in one way or another in my learning experience. In particular, Leslie Czaia, for preparing several of the crystals used in our experiments, for patiently sharing her talents in crystal processing techniques, and for guiding us through the hidden nooks of our laboratories.

CONTENTS

FIGURES

Figure

CHAPTER 1:

INTRODUCTION

1.1. MOTIVATION

The inherently parallel nature of optical information processing, coupled with its typically higher bandwidth, confers a potential advantage over conventional electronically-based processing, such as digital signal processing. Photorefractive media store real-time holograms which have memory and can provide high optical gain (20 cm^{-1}) at moderately low intensities on the order of W/cm^2, characteristics which are useful in the implementation of optical information processing architectures. Photorefractive-based systems can be subdivided in three main categories: optical computing, image processing and signal processing. Examples of optical computing systems include associative memories and correlators [Gabor, '69; Khoury, '94; Neifeld, '93; Staebler, '75; Yu, '94], neural networks [Denz, '99; Gu, '93; Psaltis, '88], and reconfigurable array interconnects [Anderson, '87; Marrakchi, '90; Weiss, '89]. Image processing systems include functions such as image amplification [Hong, '90], image thresholding [Klein, '86a; Sayano, '88], edge enhancement [Feinberg, '80; Joseph, '92], amplifying spatial filtering [Chang, '90; Fainman, '86], novelty filters [Anderson, '89; Khoury, '91; Uesu, '95]. Narrow-band filters [Hong, '93; Rakuljic, '93] and optical heterodyning [Hamel de Monchenault, '88; Khoury, '93] are examples of signal processing systems. Photorefractive systems applications have been reviewed in [Gunter, '88].

The emphasis in our research group is to perform information processing by use of photorefractive oscillating architectures which we call “rings”, such as the flip-flop [Anderson, '91], the bistable ring [Lininger, '90], the demultiplexer [Saffman, '91], and the feature extractor [Anderson, '92]. These demonstrations are described as “self-organized”, for the reasons that no external programming of the photorefractive ring is needed, nor is any *a priori* information about the input signals, except for the requirement that they be both temporally and spatially orthogonal. The dynamics of a ring oscillator generate real-time volume holograms in the photorefractive crystals which we call gratings. The competition dynamics between the generated gratings allow for different algorithms, such as separating temporally uncorrelated signals in different rings in the demultiplexer, or extracting the principal component within the input signals in the feature extractor.

This thesis focuses upon a fundamental functional unit in photorefractive processing: the two-beam coupling interaction. It is the main functional unit from which the ring systems are built, and it is also used in many of the more general applications mentioned above, such as in image amplifiers, novelty filters, notch filters, and others.

The next couple chapters in this thesis are motivated by the importance of developing a more component oriented technology for photorefractive functions, as it will significantly contribute to making photorefractive system testing and building more practical. Its widespread use in photorefractive systems justifies the choice of two-beam coupling as the example-function for testing such technology. Naturally, the same concept can be used for other photorefractive functions as well, such as

phase conjugation or four-wave mixing. The role that the development of such a component technology could represent to photorefractive systems can be illustrated by drawing an analogy with electronic systems, where systems can be assembled by the use of chips with a wide variety of function, canceling the need of building the system from the transistor level. For this purpose, in chapter 2, we introduce a modular design, where each module is pre-aligned to perform a particular photorefractive function, and the modules are interconnected by multimode optical fibers. Such technology allows systems containing several modules to be easily assembled and re-configured without the need of any system alignment. Each module is built for a specific desired function – a two-beam coupling module built for gain will be optimized differently than one built for novelty filtering. In the end of chapter 2, we give an application example using such modules. There we show how their use allowed a quick and easy verification of the change in behavior of a ring system when an extra module is inserted into its feedback loop, sparing the need for tedious realignment on the conventional optical table.

In chapter 3, we introduce the use of spherical photorefractive crystals. Their original purpose was in developing more compact two-beam coupling units. Due to the curvature and high refractive index of the crystal, no other optical elements are necessary for these modules except for the input and output fibers and the crystal itself. A built example of such module is shown herein. Interestingly, when testing the spherical crystals, we found that a single pump beam generated oscillating patterns within the crystal. These patterns arise from total internal reflections within the crystal, forming closed-path oscillating modes, known as whispering-gallery

modes. A spherical disk, an equatorial slice of the sphere containing the crystal's uniaxis, the "c-axis", was produced to allow better visualization of the patterns. The occurrence of the strongest mode, the triangle pattern, was mapped as a function of pump input and c-axis angles. A simple theory, assuming pumping of the modes by means of a single two-beam coupling interaction, resulted in good qualitative agreement with the experimentally obtained mapping. Due to the lack of a phase conjugate of the pump-beam, we believe that the oscillations are unidirectional, meaning that these structures are miniature analogous of unidirectional ring oscillators pumped by a two-beam coupling interaction, which is the architecture used for several of our signal processing systems, such as the feature extractor.

As mentioned above, the ring processors developed in our laboratories typically require that the input signals be temporally and spatially orthogonal. However, when using electrooptic modulators to impose a temporal signal upon different optical beams, the signals in these beams will have a correlation term due to the common carrier. Therefore, for the ring processor to function properly, it becomes necessary to remove the optical carrier from each signal beam. This is the case for a system being currently developed, the "optically-smart antenna array", which we describe in more detail in chapter 4. This system contains a feature extractor, currently renamed as the "autotuning filter", whose purpose is to select the strongest signal within the several signals presented at its input. Because the optical signals in this system are generated by using an electrooptic modulator, for the reason just explained above, a carrier suppressor is needed in front of the filter's input. Once again, two-beam coupling proves its versatility by performing adaptive carrier

suppression when used in a novelty-filter configuration. Carrier suppression of more then 70 dB is demonstrated. Such results were possible due to the development of an operator formalism which is the subject of the last chapter. In chapter 4, we provide a simplified, geometrical picture of this operator theory applied to the carrier suppression problem. This geometrical picture provided a greater intuitive understanding of the suppression mechanism, and allowed us to set the parameters involved in the carrier suppressor, such as input intensity ratio of the beams and the modulation strength.

Finally, the last chapter describes the operator algebra formulation for two-beam coupling. In 1979, Kuktarev published a theoretical model for beam coupling which employed coupled wave theory [Kogelnik, '69] taking into account the effect of self-diffraction of light induced gratings. [Kukhtarev, '79] The equations presented in the next section are based on the plane-wave approximation to this theory, considered the foundation for two-beam coupling modeling. However, as the number of plane-waves interfering in the crystal increases, this theory becomes increasingly more difficult and awkward to deal with. A generalized operator algebraic theory, for which the input beams can be cast not only on a plane-wave basis, but on any set of orthogonal spatial bases is then indicated. The operator theory presented in chapter 5 treats the photorefractive medium as a black box described by a coupling operator T, which acts upon an input field vector to produce the output field vector, $\boldsymbol{E}(out)=T\,\boldsymbol{E}(in)$. The field vectors are represented in whichever basis is better suited to the information processing task at hand. Due to this freedom in representing the information, the operator theory bridges a gap between the physics of two-beam

coupling and its theoretical-computational representation, leading to a deeper intuitive understanding of the beam coupling phenomena. In fact, this is exemplified in chapter 4, section 4.4, where a geometrical picture of the operator formalism led to the prediction of carrier suppression features by simply graphically representing the field vectors and studying the action of *T* upon these vectors. In the last chapter, we present the analytical solution for the coupling matrix *T* for the case of one spatial mode in each of the two input beams. We present the "complex-coupling" solution, which corresponds to the general case consisting of a combination of intensity coupling (real case) and phase coupling (imaginary case).

Before proceeding to chapter 2, in the next section we present a brief summary of two-beam coupling, for those readers who are not familiar with the process.

1.2. TWO-BEAM COUPLING: AN OVERVIEW

This overview is just that, an overview, where an effort is made to only cover the main aspects of two-beam coupling necessary for the understanding of the following chapters. We explain the physical phenomenon behind the two-beam coupling process and introduce the two-beam coupling equations. For more detailed accounts we refer the reader to [Solymar, '96; Yeh, '93].

Two-beam coupling is a nonlinear optical interaction that can transfer energy or phase information between two overlapping beams in a photorefractive medium.

The two-beam coupling medium of this thesis is always an electrically unbiased, open-circuit, barium titanate ($BaTiO_3$) crystal, where the charge transport is primarily due to diffusion, resulting in a pure energy transfer process [Buse, '97]. Barium titanate displays high two-beam coupling gain over a wide wavelength range. (Barium titanate is a perovskite ferroelectric material belonging to the 4mm crystallographic group symmetry. It's photorefractive properties are widely available in the literature. [Klein, '86b; Mazur, '99].)

A two-beam coupling diagram is shown in figure 1.1. Two beams cross inside a crystal forming an interference pattern, which is sinusoidal if the beams are assumed to be plane waves. The bright regions of the interference pattern can excite charge carriers from impurity donors, typically iron ions (Fe^{2+} and Fe^{3+}) in barium titanate, to the conduction band. In this model we assume the only charge carriers are electrons. The electrons in the conduction band are free to migrate whereas the ionized donors are fixed to the crystal lattice. Electrons may experience several transitions as they migrate, in other words, they are re-combined with the ionized donors and re-excited to the conduction band. Because the excitation of the electron is proportional to the light intensity, more electrons are generated in the bright regions as opposed to the dark regions of the interference pattern. This causes an average migration or diffusion of electrons to the dark regions. This charge separation results in a charge density function (ρ) with the same periodicity of the interference pattern, as shown in figure 1.2. The charge density and the resulting space-charge field (E_{SC}) are related by Poisson's equation, $\varepsilon E_{SC} = \rho$, which introduces a 90° phase shift between ρ and E_{SC}.

Barium titanate displays a strong linear electrooptic effect, also known as Pockel's effect, which generates a refraction index grating in the medium which mimics the space-charge field. The optical fields which originally recorded this grating will now scatter from it, i.e., the fields experience self-diffraction. The 90° phase shift between the index grating and the interference pattern causes the diffracted beams to interfere constructively in one output direction (along the "gain beam") and destructively in the other output direction (along the "loss beam"). This results in an energy transfer between the beams. The direction of energy transfer is determined by the crystal's optical axis. We designate the beam that loses energy as the "loss beam", and the one that gains energy, the "gain beam". For a given purpose, sometimes the gain beam is the pump, sometimes it is the signal. Typically it is easier to follow the pump and signal paths, though the gain and loss never change.

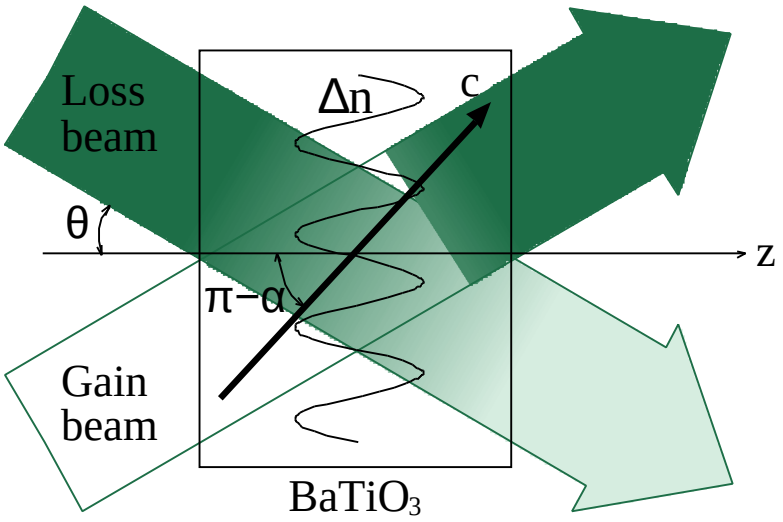

Figure 1.1. Two-beam coupling diagram. Loss beam transfers energy to gain beam. The direction of energy transfer is determined by the c-axis direction and the sign of the charge carriers. Higher gray level saturation implies brightness of the beams.

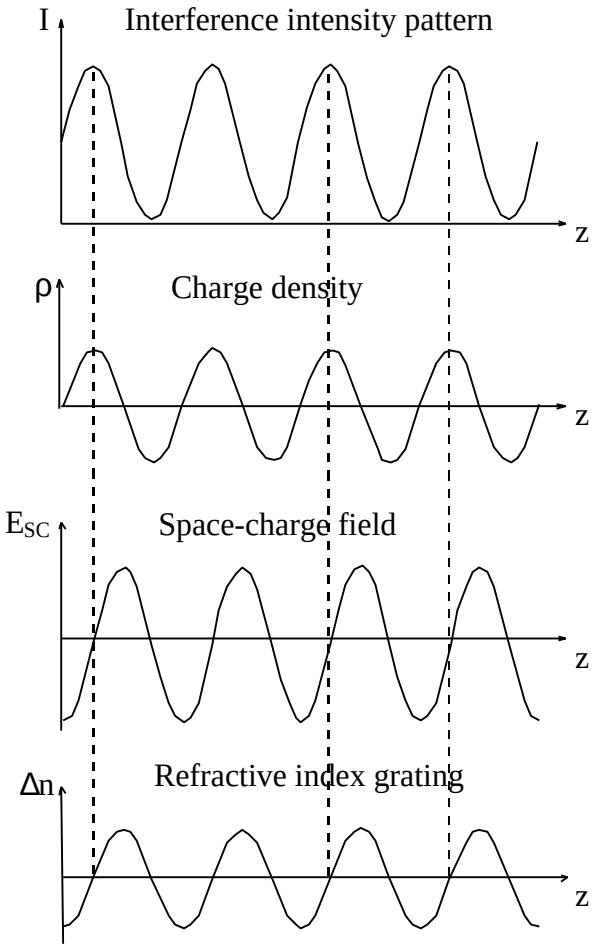

Figure 1.2. The photorefractive effect. The intensity pattern from two interfering beams create a charge separation with the same periodicity and shape as the intensity variation. The associated space-charge field, which is shifted by 90° when no external fields are applied, induces an index grating in the medium via the linear electrooptic effect (Pockel's effect).

In steady-state, the energy transfer process is represented by the following two-beam coupling differential equations with respect to the propagation direction *z*:

$$\begin{cases} \dfrac{dA_1}{dz} = G\,A_2 \\ \dfrac{dA_2}{dz} = -G\,A_1 \end{cases} \qquad [1.1]$$

where G represents the grating strength:

$$G = \frac{1}{2\,I_0}\gamma\,A_1 A_2^*, \qquad [1.2]$$

and $I_0 = |A_1|^2 + |A_2|^2$ is the total intensity. The gain coefficient γ depends upon the material properties of the crystal and upon the geometrical arrangement of the setup, and is given by:

$$\gamma = \frac{2\pi}{n\lambda\cos\theta}\,r_{eff}, \quad \text{where} \quad r_{eff} = -2\,n_o^2 n_e^2\,r_{42}\,E_{sc}(\theta,\alpha)\cos\alpha\sin(2\alpha). \qquad [1.3]$$

In the expression above, r_{eff} is the effective electrooptic coefficient, λ is the wavelength in air of the input beams, θ is the half-angle between the two beams, α is the angle between the beams's bisector and the c-axis, and n_o and n_e, the ordinary and extraordinary index of refraction ($n_o \approx 2.437$, $n_e \approx 2.365$). The r_{eff} depends on the polarization state of the fields. In this treatment we only take into account the main component of barium titanate's electrooptic tensor (r_{42}=1640 at low frequencies), since the other components are more than one order of magnitude smaller. For

extraordinary fields, this term is proportional to $\cos\alpha\sin 2\alpha$. Additionally, the space-charge field is a function of both θ and α.

$$E_{SC} = \frac{iK\dfrac{k_B T}{q}}{1+\dfrac{K^2}{k_D^2}} \qquad [1.4]$$

It depends on θ through the wave vector $K = \frac{4\pi n}{\lambda}\sin\theta$, and on α through the Debye screening length Λ_D, which in turn depends on the effective dielectric constant $\langle\ \rangle = {}_{//}\cos^2\alpha + \ \sin^2\alpha$, where ${}_{//}$ and are the DC dielectric constant for an electric field parallel and perpendicular to the c-axis, respectively. Barium titanate displays a high dielectric anisotropy with ${}_{//} = 135$ and $= 3600$.

Solving the above equations, we get the following expressions for the intensities of the gain-beam I_1 and the loss-beam I_2:

$$\begin{cases} I_1(z) = I_1(0)\dfrac{1+m}{1+me^{-\gamma z}} \\ I_2(z) = I_2(0)\dfrac{1+m^{-1}}{1+m^{-1}e^{\gamma z}} \end{cases} \qquad [1.5]$$

where *m* is the input intensity ratio $I_2(0)/ I_1(0)$.

Using the above equations, we plot in figure 1.3 the gain and loss beam intensities as they propagate through the crystal, for different values of the gain coefficient, 5, 10 and 20 cm^{-1}, and a input intensity ratio of 100. As expected, energy transfer occurs earlier for higher gain coefficients.

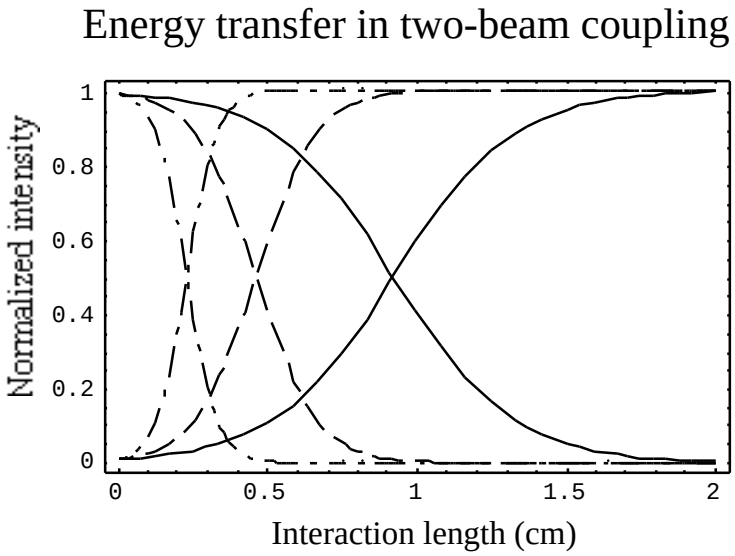

Figure 1.3. Normalized intensity plots of gain and loss beam pairs, $I_1(z)$ and $I_s(z)$ for γ=5 cm^{-1} (solid curve), 10 cm^{-1} (dashed curve), and 20 cm^{-1} (dash-dot curve). The input intensity ratio is set at 100.

Besides the gain, two other parameters are important for evaluating coupling process. The first one is losses, which can be divided into passive losses and active losses. Passive losses are due to surface reflections and absorption in the crystal. Absorption is not taken into account in the above expressions. To account for it, one simply multiplies equations [1.5] by $e^{-\alpha z}$, where α is the absorption coefficient. The curves in figure 1.3 would then be weighed by an exponential decay as they propagate in *z*. The active losses are due to scattered light from impurities and defects from the crystal, which are amplified by the photorefractive gain, forming what is called “fanning”. A picture of fanning simulation is shown in figure 1.4, after the work from [Zozulya, '95]. The losses due to fanning may be reduced by aligning the crystal in the direction of the beam fan, but the trade-off is reduced output signal dynamic range.

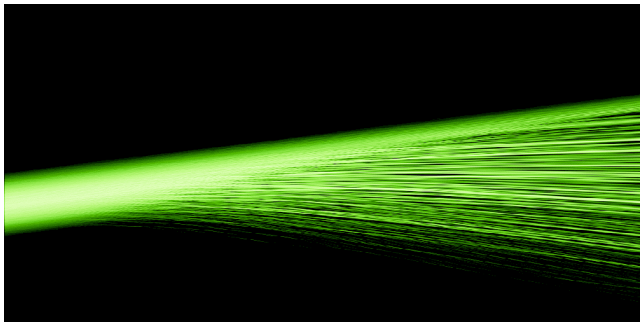

Figure 1.4. Spatial structure of fanning light inside a crystal.

The gratings in a photorefractive crystal adapts to the average input signals integrated over the time constant (τ) of the crystal. The inverse time constant of barium titanate is typically between 1-100 Hz. One might question whether such a slow response doesn't significantly limit the applicability of the photorefractive processors. In some applications, such as phase-conjugation, reconfigurable interconnections and in some image processing systems, a fast photorefractive response is desirable. However, for our applications the slow response time is not a limiting factor, but in fact actually advantageous as it allows signals which are merely 1/τ apart in frequency to be distinguished by the system. In some of these applications, the slow time constant results in long term statistical correlations which allow the system to distinguish even between signals with overlapping bandwidths. For instance, the signals could consist of speech. The speech from a particular person may vary on a short-time scale, however, on a longer time scale a person's speech is more correlated with itself than with another's, which is the key property that allows the speakers to be separated [Min, '88]. On the other end, the upper frequency limit

for the signals in the photorefractive processors is given by Bragg matching considerations and is a few gigahertz for a 1 cm grating. This limit is inversely proportional to the grating length.

CHAPTER 2:

TWO-BEAM-COUPLING MODULES

2.1. INTRODUCTION

The development of photorefractive processing systems, consisting of two or more photorefractive elements, is stymied by the lack of a well-developed component technology which would allow for rapid proof-of-concepts and testing of systems without the burden of extensive, time-consuming element-by-element alignment, as is the case of conventional photorefractive systems.

As a first step towards the development of photorefractive component technology, we developed modular photorefractive units that could be easily interconnected by the use of multimode, optical fibers. The main idea is to have the photorefractive crystal within a module and its associated fiber optic elements optimized for a specific photorefractive function and then permanently fixed in place. The modules are connectorized, and may be interconnected with multimode fibers in any desired configuration. Thus, the assembly of a complete optical system never entails alignment of beams through crystals or other optical elements which are part of each photorefractive function. This means that, with a collection of appropriate modules in hand, a complex system can be quickly assembled or reconfigured.

The geometry of each module can be optimized to perform any of the common wave-mixing effects that have found their way into conceptual and real processing systems, such as two-beam coupling gain [Khuktarev,'79], novelty filtering [Anderson,'89;Horowitz,'91a], four-wave mixing [Cronin-Golomb,'84;Feinberg,'83], self- and mutually-pumped phase conjugation [Feinberg,'82;Sharp,'94;Yeh,'92], photorefractive oscillation [Anderson,'92;White,'82;Yeh,'85], and more. Because it is employed ubiquitously in the photorefractive systems developed in our laboratory, two-beam coupling is the function of choice to test the modular concept.

To this end we have built several two-beam coupling photorefractive modules, such as the one shown in figure 2.1. This chapter discusses the development of these two-beam coupling modules, starting with design considerations, followed by the alignment procedure and the resulting characterization parameters. In the last section of the chapter we test the performance of the modules when these are interconnected to form a photorefractive system, namely an auto-tuning filter, the functioning of which is explained in that section.

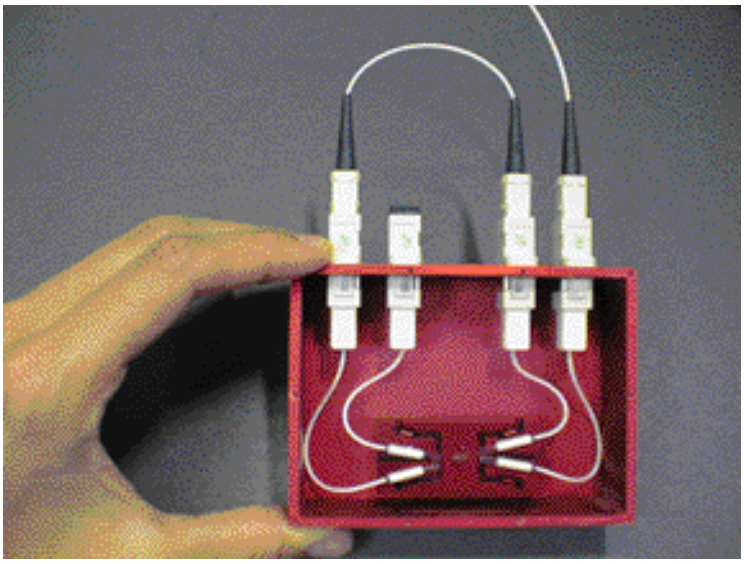

Figure 2.1. Two-beam coupling module. The picture shows a ring oscillator which is obtained by simply using an optical fiber to connect the output signal port (gain port) to the input signal port. Another fiber provides the input pump.

2.2. THE MULTIMODE FIBER OPTICS INTERCONNECTIONS

A basic step in designing a component technology for photorefractive systems is determining the kind of interconnections that should be used. The choice is basically between using free-space optics or fiber optics. Multimode fiber optics was selected because, as mentioned above, the use of connectorized fibers dispenses with the need for alignment between modules, therefore offering enormous benefit of ease of assembly and reconfiguration. In addition, the fiber-interconnected modules derive benefits from the substantially well-developed multimode fiber component technology, which provides us with standardized connectors and a gamut of fiber

terminated optical devices. What are the tradeoffs of such benefits? This brief section clarifies the way in which the use of multimode fibers affects the modules.

One major drawback of multimode fibers as opposed to free-space, Gaussian beams is that two-beam coupling gain is reduced, partly because of the nature of speckled beams [Zel'dovich,'95] and partly because of polarization scrambling by the fiber. The electro-optic coefficients in barium titanate are such that the ordinary component of the incident light polarization experiences a negligible two-beam coupling gain, and in addition, it partially erases the grating associated with the extraordinary component. This causes a reduction of the modulation index and, therefore, the gain. Polarization effects can be mitigated by adding small polarizers to the modules, but in our modules we simply accept the sacrifice in gain for the sake of simplicity.

Multimode fibers were used as opposed to single mode, not only because it is much easier to couple a beam into it as compared with the latter, but most importantly, because a multiplicity of modes are necessary for image processing applications, and other photorefractive signal processing applications as well, such as the autotuning filter described in the end of this chapter. A common misconception regarding the multimode fiber optics interconnections is that its use excludes the modules from image processing applications. This is not generally the case. The multimode optical fiber interconnections permit one to process two-dimensional spatial information. Naturally, two-dimensional data becomes scrambled as it propagates down the fiber, however the information contained in the data is preserved provided there are no severely mode-dependent losses. Many image-processing tasks

and algorithms, such as sorting or pattern recognition, are indifferent to scrambling, i.e., the presence of an unscrambled version of the processed image in the output of a system is not essential to its function. Nevertheless, if the unscrambled output image is desired, one can recover such image by holographically correlating the speckle-field output, the scrambled output image, of a fiber-based system with the unscrambled input images. Even if the application is intolerant of scrambling, the fiber-interconnected modular approach may still allow one to explore processing concepts en route to the design of a specialized optical circuit.

Our graded-index fiber interconnections have a 62.5μm core diameter and 125μm cladding diameter. If its numerical aperture of about 0.26 is filled, the fiber will contain on the order of 16,000 modes if illuminated with a 514 nm laser.

2.3. DESIGNS AND RESULTS

As shown in figure 2.1, a two-beam coupling module consists of a barium titanate crystal located in the center of a monolithic aluminum base, and in between two pairs of collets, one input and one output pair. An interbeam angle of about 15° is theoretically calculated to provide maximum gain for barium titanate, however, given the collet's diameter of 3 mm, the interbeam angle between the two collets in a pair is chosen to be 30° as a trade-off to reduce the module's length to about 50 mm. Each collet lies on an independent flexured platform which can be tilted to compensate for small fabrication errors in the parts. This tilt is adjusted by set screws accessible from

the bottom of the base (see figure 2.2). We have tested several base versions with different designs for the flexures and corresponding tilt adjustments.

A top and side view schematic of a module is given in figure 2.2. Two laser beams enter the unit via optical fibers, are collimated by the lenses in the input collets, and then cross in the crystal where they undergo photorefractive two-beam coupling. After traversing the crystal, the loss and gain beams are collected by lenses in the two output collets and focused into another pair of optical fibers. The input and output fibers are terminated with connectors, and the base, along with the connectorized fibers, are assembled in a box, (as shown in figure 2.1).

This design of the modular units optimizes the photorefractive crystal geometry. Small beam diameters between 100 μm to 820 μm allow for small crystals and an efficient use of crystal volume: the length of the crystals typically varies between 2.5 and 4 mm, the cross-section is about $(1.5\ \text{mm})^2$. We get roughly 8 module crystals from a typical $(5\ \text{mm})^3$ barium titanate piece with the appropriate c-axis direction.

We have tested several modules with different combination of base designs, lenses and crystal cuts. Below we discuss the original design followed by our improved, latest design.

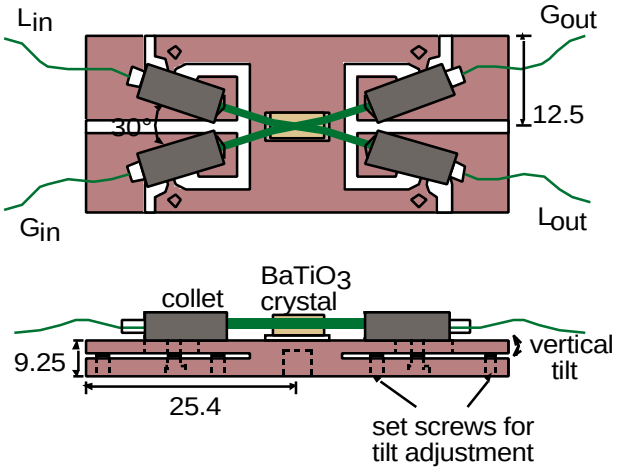

Figure 2.2. Schematic with top and side view of two-beam coupling module. A $BaTiO_3$ crystal is placed at the center of the unit over a small glass mount. Collets lie on platforms whose vertical tilt can be adjusted by two set screws. Dimensions are in millimeters.

2.3.1. The original design

The original modules contain the collet design described below and rectangular crystals.

A cross-section of a collet is shown in figure 2.3. The collets contain a 2mm-focal-length aspheric lens (350150 GelTech) which is glued to the collet with UV curing optical adhesive. A 62.5 µm core diameter fiber is inserted into a ferrule, attached with epoxy, and its end polished flush with the ferrule's face to provide an optical quality surface. The prepared ferrule is then inserted into the collet and a specially designed tool, which moves the collet-lens assembly with respect to the

ferrule, is used to collimate a 514 nm laser beam exiting the lens. The two pieces are then fixed with epoxy. The resulting beam diameter is approximately 820 µm.

The crystals were rectangular with a 20° or 30° cut with respect to the crystal axis. Maximum gain is typically achieved for a 45° cut, however the benefit of such gain maximum is associated with unwanted fanning. [Zozulya, A.,'95] Fanning reduces the dynamic range of the two-beam-coupling module, but the effect can be ameliorated by simply reducing the crystal-cut angle, which reduces the gain. The crystal-cut must be tailored to the application at hand. For the applications in our laboratories, high gain is typically desired so the 30°-cut crystals were more successful. All crystals were approximately 4 x 2 x 1.5 mm^3.

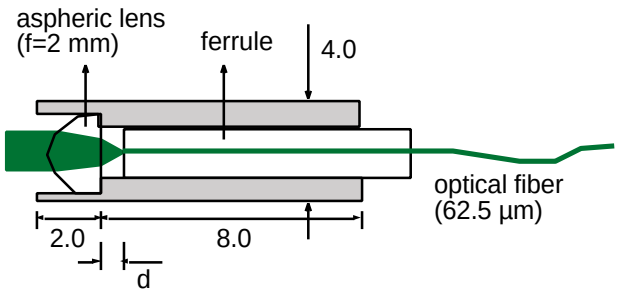

Figure 2.3. Cross-section of a collet with an aspheric lens (Geltech, 350150). The zirconia ferrule contains a polished multimode fiber with 62.5 µm core and 125 µm cladding. Distance d is adjusted to collimate the outgoing beam. All unspecified dimensions are in millimeters.

2.3.1.1. The alignment procedure

The alignment procedure, as depicted in figure 2.4, begins by mounting the module base on a rotation stage, and placing the crystal on a glass spacer at the center of the base. Next, each of two collets is attached to a jig. The jig consists of a two-dimensional translation stage with an extension arm with a beryllium-copper spring at the end, to which the collet is attached. The collets are positioned 30° apart at the input side of the base. They are made to completely contact the base by having the jig exert a light pressure upon them. With this arrangement a collet has four adjustment degrees of freedom: longitudinal and transversal translation, rotation about the axis through the center of the base and perpendicular to it, which we call “horizontal rotation”, and the “vertical tilt” provided by the flexured base. (The translation and horizontal rotation stage are shown in figure 2.4, whereas the vertical tilt, in figure 2.2).

Optimization of the photorefractive gain is the main goal in aligning the input collets. To do this 514nm Argon-Ion laser light is coupled into the input fibers and the overlap of the two beams inside the crystal is then maximized. This is accomplished by use of the longitudinal and transversal translation, and the vertical tilt. (Horizontal rotation is only needed when aligning the output collets.) Typically the gain is not uniform throughout the crystal’s volume. [MacCormack,'96] Therefore, one can search for a higher gain by simply moving the crystal sideways, so that the beam overlap probes different regions inside the crystal, and then select a particularly good position. To avoid problems when coupling into the output collets,

the beams must be parallel to the plane of the base. Once the optimal gain is obtained, the crystal and input collets are fixed to the base with epoxy and the jigs are removed.

The same pair of jigs are now used to position the two output collets to optimize the coupling of each beam into the respective output fiber. Finally, the two input and two output fibers are cleaved and terminated in SC connectors and the unit is enclosed in a 10.16 x 7.62 x 3.25 cm^3 box.

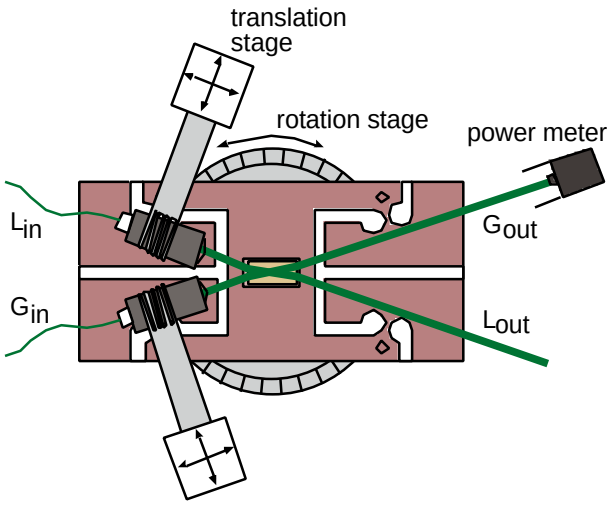

Figure 2.4. Setup for the alignment of the input collets. The gain is optimized by adjusting the translation stages and the set screws shown in figure 2. The rotational stage is used during the alignment of the output collets.

2.3.1.2.Results

Three quantities characterize these modules: gain, passive loss, and time response.

The gain is measured by taking the ratio of the output intensity of the gain-beam with the loss-beam unblocked over that with the loss-beam blocked. The gain measurements were obtained with an input intensity ratio of the loss-beam over the gain-beam of 3000. Three modules were built with 20°-cut crystals and they had gains of 12, 13 and 19, and another three were built with 30°-cut crystals having gains of 286, 406 and 435.

The passive losses are given by subtracting the passive signal coupling from one. The passive signal coupling was measured by taking the output to input intensity ratio of the gain beam while wiggling the fibers so as to impede the formation of photorefractive gratings in the crystal. The passive losses ranged from 72% to 84%, with an 80% average. We also measured a significant deterioration of the passive signal coupling due to alignment drift with a time scale of weeks. One of the modules passive losses went from 72% to 86% in about a month, whereas two other modules were completely misaligned after the same period.

To test the response time of the modules, we presented a step function to the input and measured the 10 to 90% rise time in the output. The input approximation to a step function, with a rise time of about 5 ms, was generated by manually unblocking the input gain beam. The measurements were performed with a loss beam power of 100 mW and a gain beam intensity of approximately 1% that of the loss beam. The output rise time was always between 500 and 700 ms.

2.3.2. The next generation

This section discusses, based on the above measured results, the routes for improving the module's design towards a new generation. Our primary concern is to reduce the passive losses and, most importantly, to improve the degradation with time of the passive signal coupling due to an alignment drift. Below we list the modifications made in the new design. The alignment procedure is similar to that of the first generation (section 2.3.1.1). The last subsection gives the results for the next-generation modules.

2.3.2.1. A new base design

A top view schematic of the original base is shown in figure 2.5 (a). We call attention to the pivot points of the four flexured platforms. In this original base design, the pivots are wider vertically than horizontally (where horizontal is the plane parallel to the paper in the figure). We'll therefore designate these pivots as "vertical pivots". In some occasions the platforms pivots broke off during the modules' alignment procedure (see section 2.3.1.1 above). This happened because the height adjustment of the flexured platforms provided by these vertical pivots are insufficient for correcting nonidealities of the components in the modules. For instance, the crystal faces are not perfectly parallel, which cause the beams to be deflected. This suggests that the pivots could be significantly mechanically stressed even when they

didn't break. And most importantly, such stress is very likely the culprit for the alignment drift as the aluminum tries to relax.

To ameliorate the mechanical stress we tested several different base design modifications. The chosen design is the one shown in figure 2.5 (b), which is similar to the original, but instead of a vertical pivot it has a horizontal pivot (meaning that the pivot is wide in the horizontal plane and thin in the vertical plane). These allow for more range of height adjustment without sacrificing the tilt adjustment.

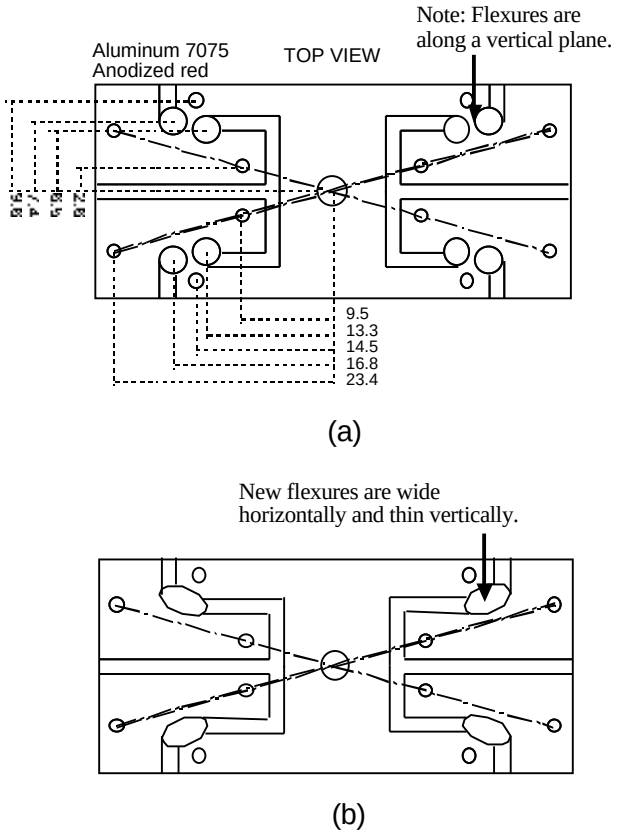

Figure 2.5. Details of the base design. Dimensions are in millimeters. (a) Original design with vertical pivots. (b) New base design is similar to the original, but with horizontal pivots which allows for greater

adjustment range. The ellipses represent milled slots resulting on wide but thin (about 750 μm) flexures.

2.3.2.2. Brewster-cut crystal

As explained in section 2.2 above, the ordinary (vertical) polarization partially erases the grating, reducing the gain. For two-beam coupling application, the greatest component of the unwanted vertical polarized light typically comes from the pump. So we designed a new "Brewster-cut" crystal geometry as shown in figure 2.6. The Brewster angle for barium titanate is 67°, and is obtained by neglecting the crystal's anisotropy and using an refractive index of 2.4. Having the pump beam enter the crystal at Brewster's angle increases the loss of the vertical polarization component to about 50%, while reducing the desired horizontal polarization component loss to less than 2%. The average reflection loss of the signal at 37° (such that angle of pump minus signal is 30°) is about the same as that at zero degrees, i.e. about 17%. Also, because the pump beam comes in at a steeper angle, it is wider inside the crystal than the signal beam: this facilitates alignment optimization for two-beam coupling. To reduce absorption losses, the new Brewster-cut crystals are 2.5 mm long, as opposed to the previous 4 mm length of the older rectangular crystals. The optical axis of the new crystals are oriented at 45° with respect to the input surfaces.

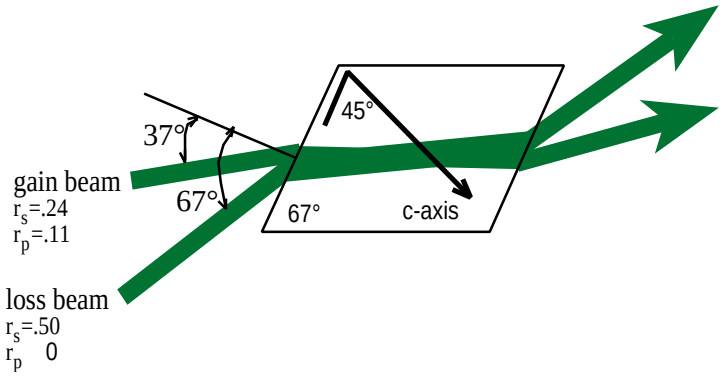

Figure 2.6. Top view of Brewster-cut crystal.

2.3.2.3. Graded-index lenses

Cheaper than the aspheric lenses, the graded-index (GRIN) lenses come in more variety, are easier to assemble, and dispense the use of collets or other mounts since they can be glued directly to the ferrule using optical adhesive for index matching. Figure 2.7 below shows a cross-section of the new ferrule-lens assembly. It is assembled by using a V-groove mount to align the center of the lens to that of the ferrule while curing the optical adhesive with UV light. The external end of the GRIN lenses were anti-reflection coated to reduce losses. We used a slightly focusing lens pitch (Selfoc SLW1.8 - .29 - 555 from NSG America) to decrease the beam diameter inside the crystal, resulting in beam diameters in the waist of about 100 μm. The time response of a crystal is roughly inversely proportional to the total intensity of the beams. [Horowitz,'91b] This means that the smaller beam diameters should result in a decrease in the response time of the modules.

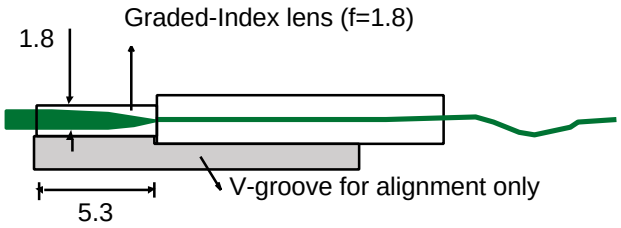

Figure 2.7. Cross section of new lens-ferrule assembly. A schematic of the v–groove is shown but it is removed after alignment. The fiber output will be imaged by the lens at a distance of about 6.3 mm from the output surface of the lens.

2.3.2.4. Buffered fibers

The optical fibers used in the first-generation modules were fibers having only a 245 µm diameter coating over its 125 µm diameter cladding (62.5 µm core). The operation of the modules is sensitive to acoustic vibrations, which disturb the fibers, change the speckle configuration, and thereby affect the two-beam coupling grating. When the modules are tested in a ring configuration such vibrations cause the so called “breathing” in the output, meaning that the output would slowly turn on and off. To ameliorate this effect, we switched to fibers having a 900 µm buffer jacket which helps isolate them from external vibrations. The buffered fiber also has the advantage of greater mechanical resistance, are white, and therefore are easy to see in a darkened room. Not only did we use these buffered fibers in some of our new

modules, but also, and perhaps most importantly, we used them in all the new module-to-module fiber cables.

2.3.2.5. Results for the new generation

We built a total of 3 modules with the above modifications. These modules are characterized in a similar way as described for the earlier modules (see section 2.3.1.2). The resulting small-signal gains are 526, 664 and 843; the passive losses are 68%, 73% and 72%; and the 10 to 90% rise time at the output when the input is unblocked is 120, 164 and 122 msec, respectively.

The higher gain is most likely due to a combination of factors. First, the Brewster-cut crystal geometry, which, as discussed earlier, increases the gain by reducing the ordinary polarization component. Second, the gain characteristics of the particular boule from which the crystals were cut. We have very little control over the material properties of the crystals, making it hard to discern how much each of these two effects contributed to increasing the gain.

The passive-loss average of 71% is about 10% less (better) than that of the first-generation modules. This number is due to a combination of loss components. We measured the absorption coefficient for barium titanate to be about 1.7/cm, resulting in a absorption loss of 35% for a 2.5 mm crystal. The reflection losses are approximately 25%: 50% reflection loss for the ordinary polarization and 0% for the

extraordinary polarization. The remaining 11% losses are consistent with typical measured coupling losses.

The alignment drift was, unfortunately, still present, however it was much less severe than in the first-generation modules. Two months after the above loss measurements were obtained, the measurements were redone and values had changed to 80%, 87%, and 79% respectively, corresponding to an average loss increase of 11%. The loss increase for all three modules is less than the loss increase for the earlier modules.

As expected, due to the smaller beam diameter, these modules responded an order of magnitude faster than the earlier ones. (Even though the pump beam diameter is increased by the Brewster incidence angle to about 250 μm, it is still smaller than the pump beam diameter inside the crystal in the first-generation modules of 850 μm/ cos 15° = 880 μm.)

2.4. DISCUSSION AND FUTURE DESIGN

The second-generation modules provided us with higher gain, lower losses and faster response time than the previous generation. However, an alignment drift is still present, though much less severe than before. This suggests that the components of the modules are performing well, but that the base is still mechanically relaxing causing the alignment drift. We believe the cause of this relaxation is due to the spring action of the flexured platforms. Such relaxation could be enhanced by either

temperature variations or shock. Therefore, as a future project for improving the modules we suggest that a new base be designed. Below we give some suggestions for a new base design, but before that, for the benefit of possible future designers, we first estimate the errors associated with the modules' components.

If further improvement of the base design is pursued, an assessment of errors and tolerances within the module will become necessary. The main misalignment causing errors are the following: the crystal's facet perpendicularity error, typically ± .015 rad, the lens' facet perpendicularity error, ± .006 rad, offset between the center of the lens and the ferrule, and lens tilt with respect to the ferrule. The offset between the center of the lens and the fiber is due to errors in the lens and ferrule radius (± 5 μm for each), lens and ferrule nonconcentricity (negligible compared to diameter error), and the height error in the V-groove mounts used to align the lens to the ferrule (about ± 25 μm). The total offset between the lens and ferrule in the object plane ($\pm\sqrt{(2 \cdot 5^2+24^2)} = \pm 25$ μm) is magnified 3.7 times by the lens resulting in a displacement of the beam in the image plane, which occurs inside the crystal, of ± 93 μm. Given the distance of about 6 mm between the lens and the crystal, this displacement is equivalent to an angular error of approximately ± .015 rad. Finally, one edge of the lens can be higher then the opposite edge (by ± 25 μm), which will result in a lens tilt with respect to the ferrule (of ± .004 rad for the 6 mm GRIN lens). This causes an angular deviation of the out-coming beam of ± .006, calculated by using the GRIN lens ray-tracing matrix. Adding up all the contributions we get a total tilt error of $\varphi=\sqrt{(2 \cdot 015^2+2 \cdot 006^2)}= .023$ rad. The current optical length between the

coupling lenses in the module is about 10 mm, resulting in a displacement error of 230 µm, as shown in figure 2.8.

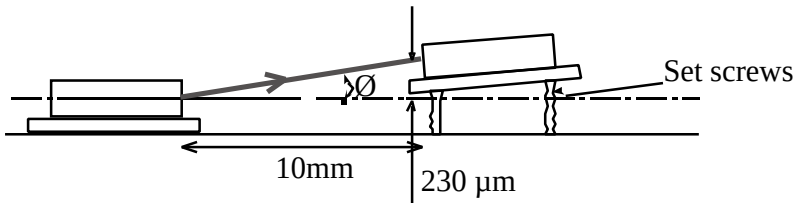

Figure 2.8. Representation of total displacement and tilt errors between lenses.

The main point in designing a new base is the following: Given that no adjustments are needed after the modules are ready, *all the adjustments should be external to the base design*. The base should serve solely to support the components, avoiding the use of internal adjustments (screws, springs, etc.), and thereby reducing the possibility of misalignment after the module is concluded. We suggest a design for the base where the crystal lies in the center of the base, shown in figure 2.9 (a). The five degrees of freedom for each collet would then be externally supplied by a "jig", a 2-D tilt stage which is held by a 3-D translation stage. The main idea is to have the base with poles or blocks that slide up to almost meet the ferrules after they have been aligned. (A design with wide blocks is preferable to one with thin poles, as it is less susceptible to vibrations.) Low shrinkage epoxy is then used to fill the small gap between the ferrules and the base by capillary action. The ferrules should not move during the capillary process as they are held fixed by the jig. The epoxy used to

fix the ferrule to the sliding blocks and the sliding block to the base should have low shrinkage coefficient and low coefficient of linear thermal expansion (CTE). It should also have a low enough viscosity (< 1000 cps) so that it can wick into the gap between the ferrule and the pole or block. One viable epoxy is EPOTHIN from Bhueler with a shrinkage coefficient of .0002, CTE of $62 \cdot 10^{-6}$/°C, and viscosity at 25°C of 200 cps. Another possibility is the EP30 from MasterBond with a shrinkage of .0003, which is slightly higher than that of the EPOTHIN but the CTE is lower, $35 \cdot 10^{-6}$/°C, approaching that of aluminum, $24 \cdot 10^{-6}$/°C, and of zirconia, $10.5 \cdot 10^{-6}$/°C, the material used in the ferrules. One could also experiment machining the base out of a material with lower thermal expansion than the currently used aluminum. There are machinable ceramics whose CTE is close to that of the zirconia, such as AREMCO 502-400 with a CTE of $10.8 \cdot 10^{-6}$/°C. The glass-ceramic material Zerodur™ is another possibility with CTE on the order of 10^{-7}/°C.

Besides a new base design, below are other possible modifications to take into consideration for a future design. Most of them involve a trade-off between gain and loss. One possible modification is to use rectangular cut crystals but with anti-reflection coatings on both input and output surfaces to reduce the reflection losses. However, that would allow both polarizations to enter the crystal and, as discussed earlier, would reduce the gain. That would also significantly increase the cost of the module. On the other hand, one could add polarizers to increase the gain. However, due to the speckle nature of the beams which scrambles the polarization, the polarizers would also increase the passive losses. Naturally, one more way to

manipulate the gain/loss trade-off is via the crystal's length, as more length implies more gain but also more absorption losses.

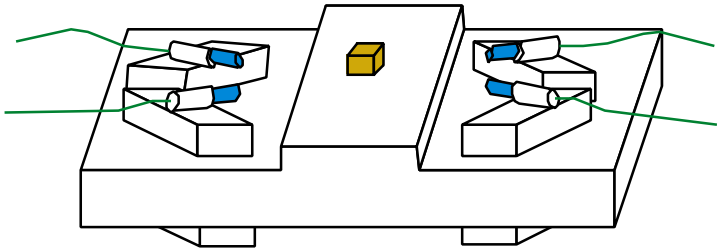

Figure 2.9. Suggestion for modular base design. Ferrule-lens assembly is adjusted externally by translational and rotational stages. Then the corresponding bases are slid upwards to meet the ferrule and glued with low shrinkage epoxy.

Finally, in a stretch of our imagination, it would be interesting if one could find a transparent liquid/gel substance which could solidify with extremely low shrinkage and without changing its refractive index. The ferrules could be positioned, with the use of pre-solidified bars of the same material, inside a mold containing the liquid material. The ferrules would then be aligned and the material in the mold solidified. Cut off the solidified bars that were originally holding the ferrules (which should now be sticking out), polish the six faces (assuming your mold was a parallelepiped) and you have it: a two-beam coupling module as a solid transparent piece (like the fossils in resin that you saw as a kid) with fibers sticking out.

2.5. AN APPLICATION EXAMPLE: THE AUTO-TUNING FILTER

Once the modules are in hand, building photorefractive circuits is trivial. The two-beam coupling modules can be quickly and easily interconnected to build and oscillator rings [Yeh,'85], reflexive-coupling units [Anderson,'95], and other systems. We tested the modules by using a ring oscillator with and without a reflexive coupling unit. This architecture is called the auto-tuning filter, an information processing system also known as the feature extractor [Zozulya, A. A.,'95], which we describe in this section as an example of the versatility provided by the modules.

Given two or more temporally and spatially orthogonal signals superimposed on a common input beam, an auto-tuning filter is a self-organizing system that learns to select the strongest input signal from within all the other input signals, in other words, it performs a principal component extraction. It consists of a photorefractive ring resonator with a common input beam as the pump. The non-linear dynamics in the crystal causes a competition of the signals for the resonator modes; the signal with the greater optical energy wins. For simplicity, only two input signals are used in our experiment. We built the auto-tuning filter system in the two different configurations shown in figure 2.10: as a simple ring oscillator and as a ring oscillator with a reflexive-coupling unit inside the ring.

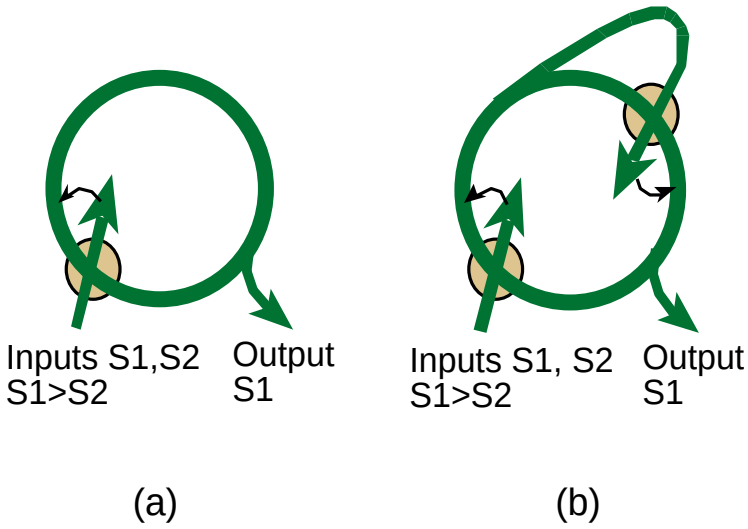

Figure 2.10. Autotuning filter in two different architectures: (a) simple ring, and (b) ring with reflexive coupling. The photorefractive crystals are represented by the circles.

Reflexive coupling [Anderson,'95] increases the competition between the signals that oscillate inside the ring, enhancing the selectivity of the auto-tuning filter. In simplified terms, the reflexive-coupling works as follow: A fixed fraction of these oscillating signals is split away from the ring and folds back to cross the ring inside the reflexive-coupling crystal. Part of these split signals are then coupled back into the ring - the strength of this coupling is dictated by the strength of the photorefractive grating written by each signal. These two signals compete for the available gain in the crystal. The weaker signal writes a weaker grating and thus experiences greater round-trip loss, which results in an even weaker signal, and so on, while the stronger signal undergoes the opposite behavior. Ideally, this positive feedback process continues until the weaker signal is totally inhibited by the stronger

one. In practice though, total inhibition of the weak signal is defeated by fanning [Zozulya, A.,'95] of the loss beam into the ring.

Figure 2.11 shows the experimental setup for the auto-tuning filter with reflexive-coupling. The laser beam is split by a polarized beam splitter; the intensity ratio of these two input beams is adjusted by the half-wave plate preceding the beam splitter. Each beam goes through an acousto-optic modulator (AOM) with 60% diffraction efficiency in the first order. The AOMs perform two functions: they shift the optical carrier frequency, resulting in a frequency separation of 280 MHz between the two input beams, which guarantees their temporal orthogonality; and they act as shutters to time modulate the optical carriers with the two input signals, single-sided square pulses at 1 kHz and 625 Hz respectively. The duty cycle of these pulses is set at 90% for low power loss. The two signal beams are then coupled into optical fibers and mixed by a directional coupler. To have the same contribution of each signal in the mixed input, a .50/.50 directional coupler is used (meaning that half of each incoming signal beam is coupled to each outgoing fiber). The beam of one of these outgoing fibers is directed to a photodiode, and the other is photorefractively coupled into the resonating modes of the ring by the pump unit, forming the oscillating beam. A second directional coupler inside the ring splits the oscillating beam so that 90% is directed into the input loss port of the reflexive-coupling, and the other 10%, into the input gain port. Finally, a third directional coupler (.01/.99) is used to sample the ring, forming the output which is monitored by a second photodiode. The intensity of the two photodiode signals are displayed on a spectrum analyzer (HP 356A, 100kHz).

The experimental setup for the simple ring oscillator is similar to that of figure 2.11 except that reflexive coupling is bypassed with an optical fiber.

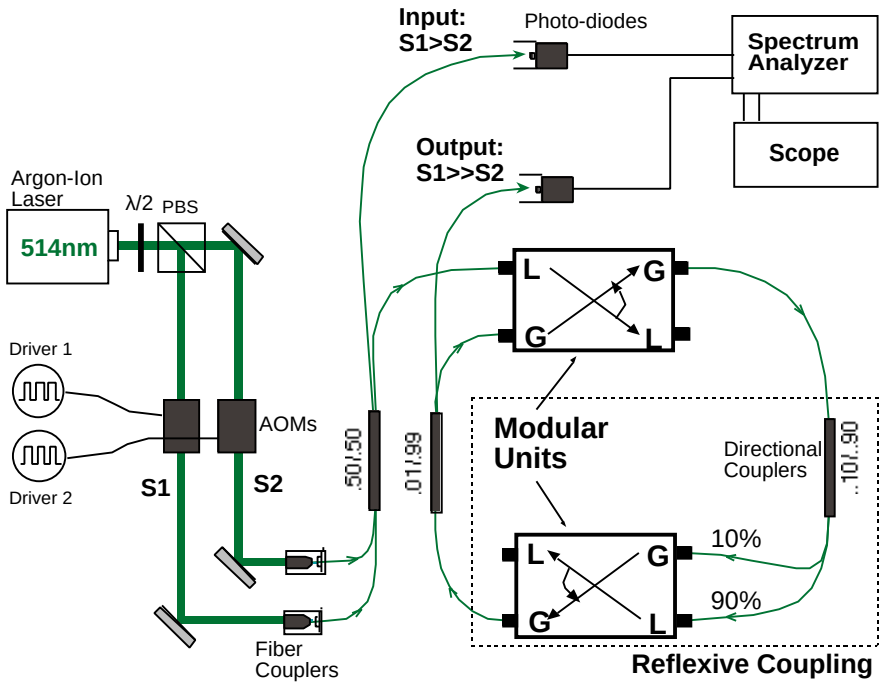

Figure 2.11. Experimental setup for the autotuning filter with reflexive coupling. The setup for the simple ring is obtained by simply bypassing the reflexive coupling. (PBS: polarized beam splitter, AOM: acoustooptic modulator.)

The effectiveness of the auto-tuning filter can be given by the contrast ratio (the strongest signal intensity over the weakest signal intensity) in the output, R_{out}, as compared to the contrast ratio in the input, R_{in}. Figure 2.12 shows the results obtained with an R_{in} of 3.17. The intensities of the input signals are shown at the top of the figures and that of the output signals, at the bottom. Figure 2.12 (a) shows the case of the ring with reflexive coupling. The resulting R_{out} is approximately 45 dB. We found

that the system could not self-start oscillation with R_{in} lower than 3.17. This is beacuse the available gain in the medium is shared by the signals, meaning that the closer R_{in} is to one, the lower the gain available to the stronger signal. Eventually, when $R_{in} < 3.17$, this effective gain becomes lower than the minimum necessary for the system to self-start.

The effect of adding the reflexive coupling to the ring can be evaluated by comparing the result in figure 2.12 (a) with that in 2.12 (b). The absence of reflexive coupling in the simple ring configuration decreases the competition between the signals, resulting in a lower contrast at the output: R_{out} is about 38 dB, 7 dB lower than with reflection coupling. On the other hand, the removal of reflexive coupling also reduces the round-trip losses, which enables the system to self-start oscillation with lower R_{in}. The simple ring could self-start with R_{in} down to 1.75.

Finally, to check for asymmetries in the system, we switched the input signals of the ring with reflexive coupling, but keeping the ratio constant. The result is shown in figure 2.12 (c). R_{out} is 43 dB, 2 dB worse than the symmetric counterpart, corresponding to a 2:3 asymmetry. We believe this asymmetry is mostly due to the mode structure dependence of the directional couplers.

(a) Ring with Reflexive Coupling:

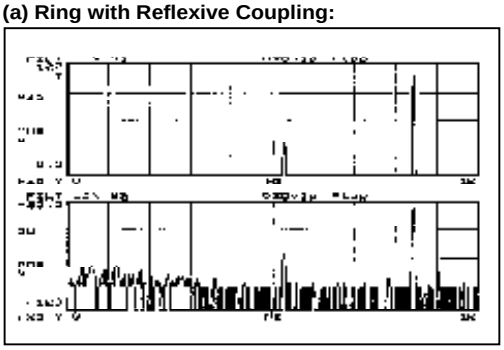

Input: S1/S2= 3.17 ± 0.1
Output: S1/S2= 45.4dB ± 1dB (34 674)

(b) Simple Ring:

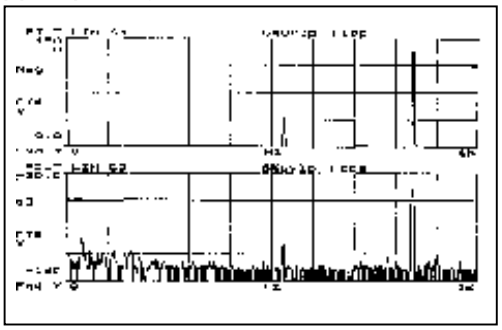

Input: S1/S2= 3.17 ± 0.1
Output: S1/S2= 38.2dB ± 1dB (6607)

(c) Ring with Reflexive Coupling (symmetric case):

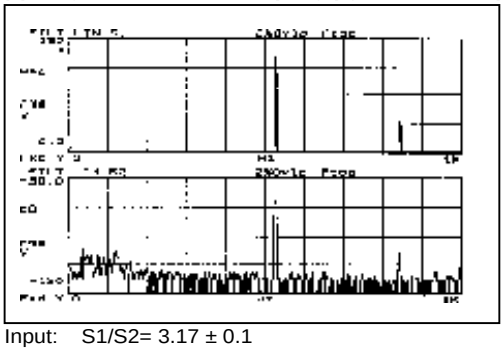

Input: S1/S2= 3.17 ± 0.1
Output: S1/S2= 42.5dB ± 1dB (17783)

Figure 2.12. Input and output intensity spectra for the autotuning filter. Input spectrum is shown at the top of each screen with a ratio of 3.17:1 between the two input signals (linear scale); output spectrum is shown at the bottom (dB scale). (a) Ring with reflexive coupling, output ratio is 45 dB; (b) simple ring, output ratio is 38 dB; and (c) same as (a), except that the input signals are switched to check for asymmetries, output ratio is 43 dB. Reflexive coupling significantly enhances the selectivity.

2.6. CONCLUSIONS

On the auto-tuning filter application above, the use of the two-beam coupling modules allowed quick verification of the properties of the system, such as the fact that adding the reflexive-coupling increases the output contrast. In this context the modules have demonstrably fulfilled its purpose of supplying a means for quick testing of concepts and of new ideas in photorefractive systems. With a collection of different modules available, complex systems can be easily assembled and modified.

The specific modular design one chooses for a particular function, such as two-beam coupling, is always subject to improvements. In this chapter, we have shown the evolution from the original two-beam coupling modular design to an improved design rendering higher gain, lower losses and less long-term alignment drift. Suggestions for a future design to further reduce the drift is also given. Eliminating the long-term drift would add system reproducibility – after a modular system is disassembled it could be re-assembled exactly as before by simply using the same modules.

When building the modules one would want to tailor it to their applications. For example, the number of modules that can be cascaded, say, within a ring, is limited by the losses. Therefore, it might be of interest to further reduce the passive losses of each module, but keeping in mind the typical trade-off between gain and loss, as discussed at the end of section 2.4.

CHAPTER 3:

BARIUM TITANATE SPHERES AND SPHERICAL DISKS

3.1. INTRODUCTION

In the last chapter we discussed the two-beam coupling modules. In this chapter we discuss an idea with the original purpose of making two-beam coupling units even more compact: that of having a spherical barium-titanate crystal as the gain medium. Due to its curvature and high index of refraction, the lensing and gain effect of a photorefractive sphere can be combined to perform fiber-to-fiber two-beam coupling, dispensing the use of external lenses. The resulting two-beam coupling units with barium-titanate spheres are described in section 3.2 below.

We also found that, due to its high photorefractive gain, it is easy to excite whispering gallery modes (WGM) within the spherical crystal by shining a single pump beam onto it. Several patterns were observed, but the lowest order mode, the triangle pattern, was found to be the most robust. The WGM patterns can be better observed and documented when excited in a spherical disk, an equatorial slab of the sphere. In section 3.3 we discuss the oscillating patterns and compare the occurrence region of the triangle patterns with that predicted by a simple theoretical model.

3.2. PREPARATION

Optical quality spheres are straightforward to produce with hand lapping and polishing techniques. [Baxter,'50] We found that barium-titanate and lithium niobate are not substantially more difficult to form into a sphere than optical glass. The barium-titanate was electrically poled in its rectangular form before processing it into a sphere. We feared that barium titanate in particular might become depoled during processing, but such was not the case. Finished spheres of photorefractive barium titanate in fact turn out to be more robust to shocks than their delicate rectangular-cut counterparts, possibly due to the lack of sharp edges or corners from which cracks could propagate.

Spherical disks were produced by first forming a sandwich of two lithium-niobate slabs surrounding a slab of barium-titanate, held together by quartz wax. The sandwich is then lapped and polished into a sphere. Upon removing the lithium-niobate end-caps one is left with a barium-titanate disk with spherical sides, with the c-axis in the plane of the disk. Unlike the sphere, it is easy to observe through the flat top of the disk the beams as they propagate inside the crystal. We produced sphere and disk sizes from 3 mm to 7 mm diameter.

The c-axis of a 0°-cut photorefractive crystal is normally found by placing the crystal between two polarizers and identifying the widely-known conoscopic “iron cross”. The lensing property of the sphere morphs the iron cross into a “beach ball” as shown in Figure 3.1, thus it is easy to find and orient the c-axis of the sphere.

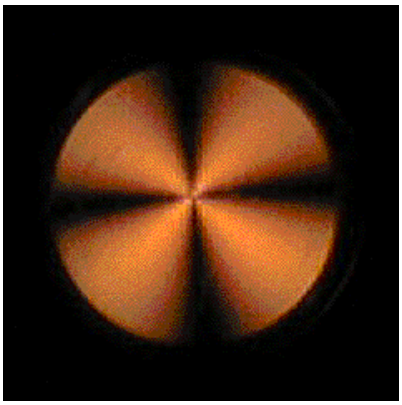

Figure 3.1. The "beach ball" pattern of a spherical photorefractive crystal between crossed polarizers observed directly along the c-axis.

3.3. TWO-BEAM COUPLING WITH SPHERES

Two-beam-coupling interaction can be made compact by taking advantage of the geometry of the spheres and the high index of refraction of barium titanate, which is greater than 2 throughout the visible spectrum. Due to these properties, the crystal can directly image the light from one optical fiber to another. In a symmetrical arrangement, the collimated beam inside the sphere can be photorefractively coupled to a second beam propagating between a second pair of fibers. Figure 3.2 shows direct fiber-to-fiber two-beam coupling using a photorefractive sphere without other intervening optical elements. The sphere conveniently magnifies the interaction region viewed by the camera. Two beams, at 514 nm wavelength, cross inside the crystal and undergo two-beam coupling. Each beam is associated with a pair of multimode gradient index fibers, with a 62.5 μm core diameter. With a spherical disk

of 4 mm diameter, the collimated size of the laser beam in the crystal is about 0.8 mm when the fiber-to-fiber imaging is optimized. The apparatus allowed rotation of the crystal axis continuously and permitted the angle between the beams to be chosen from 5° to 45° in 5° increments. Maximum gain occurred at the expected 45° between the c-axis and input beam bisector. The optimum beam angle was observed to be 10°±2.5° - larger than the 4°-6° typically estimated in theoretical plane-wave calculations. [Fainman,'86] Gain was measured using a loss-to-gain beam ratio of 10^5:1 and a gain-beam strength of 0.5 μW. As in the previous chapter, we define gain to be the ratio of the gain-beam intensity at the output of its fiber with the loss-beam present to its intensity with the loss-beam blocked. Because the light from the fibers is unpolarized, one expects an effective reduction of the coupling constant Γ by a factor of 2. We nevertheless obtained a maximum gain of 8000, which is comparable to gains obtained with rectangular-cut crystals of similar length.[1]

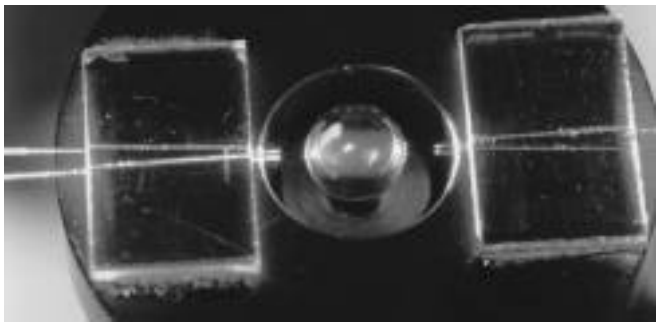

Figure 3.2. Two-beam coupling between two pairs of fibers using a spherical photorefractive crystal of barium titanate.

[1] The two-beam coupling unit was built and tested by Edeline Fotheringham.

3.4. WHISPERING-GALLERY MODE PATTERNS

We have also investigated interesting oscillation patterns that occur when a Gaussian (free-space) pump is incident on the spherical disk. The oscillating patterns are understood to be low-order whispering gallery modes which are generated by total internal reflection at the crystal's boundaries.

The modes of a spherical resonator that propagate by total-internal reflection at the surface were first analyzed by Lord Rayleigh for acoustic waves and he referred to the analysis as "The problem of the whispering gallery". [Lindsay,'70] Baer demonstrated continuous-wave active excitation of whispering gallery modes using a Nd:YAG sphere pumped with a diode laser. [Baer,'87] Demonstration of active oscillation of whispering gallery modes in a gamut of other materials (and structures) followed, such as in fused-silica [Schiller,'91], polymers [Kuwata-Gonokami,'95], semiconductors [Courtney,'98], and organic materials [Lin,'98]. In these demonstrations oscillation arises from stimulated emission, whereas in our photorefractive spheres oscillation arises from two-beam-coupling, a parametric interaction between the incident pump, the loss beam, and the modes of the resonator, the gain beams.

3.4.1. A family of patterns

At a wavelength of 532 nm, the critical angle for total internal reflection is arcsin(1/2.4), about 25°, thus the lowest order whispering gallery mode of a barium-titanate sphere or disk is a triangle. Since the maximum two-beam coupling gain for barium titanate occurs for small loss-to-gain interbeam angles, one expects the patterns to orient themselves such as to minimize this angle. As shown in figure 3.3 for the triangle and square, the interbeam angle is minimum when a vertex of the pattern aligns itself with either the incident pump location or with the pump's first reflection location. (Second and higher pump reflections are too weak to excite patterns.) We call the former "front-side" patterns (shown with full lines in figure 3.3) and the latter "back-side" patterns (shown with dashed lines). As also shown in figure 3.3, the minimum possible interbeam angle occurs for maximum displacement of the pump, giving 5° for a triangle, 20° for a square and larger for higher-order regular polygons. Since this interbeam angle is smaller for lower order patterns, and smaller interbeam angle translates into higher gain, we expect the triangle to be both the strongest oscillating mode and the easiest to excite.

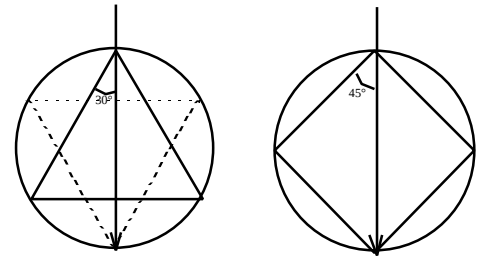

(a) φ=0°

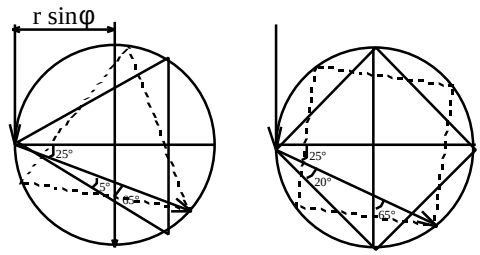

(b) φ=90°

Figure 3.3. Diagrams of minimum interbeam angles. (a) Pump propagates directly down the center of the crytal. (b) Pump is incident at maximum displacement (r sinφ) from center. In every case, the minumum interbeam angle occurs when vertices are aligned with the pump incidence location (full line triangle and square) or when vertices are aligned with pump's first reflection location (dashed line).

Our experiments reveal that this is indeed the case. The setup used for observing the oscillating patterns is shown in figure 3.4, and pictures of the patterns in figure 3.5. Figure 3.5 (a) shows a front–side oscillating triangle mode in a 5.2 mm diameter spherical disk. In the figure, the pump beam enters the crystal in the vertically downward direction. The pump beam is focused by a microscope objective so that a beam waist occurs inside the disk and is roughly matched in position with a waist of the mode. Most of the pump energy is depleted in the first millimeter after the pump enters the disk, indicating efficient energy transfer. Back-side oscillation

also occurs when the crystal c-axis is appropriately rotated. In Figure 3.5 (b) gain is provided to the triangle by the reflection of the pump off of the far-side surface. In this instance the microscope objective is adjusted to collimate the beam in the disk. The oscillation is weaker than the front-side case since the pump intensity is reduced by both absorption and transmission (causing the pump to exit the crystal).

Other modes are excited by changing the orientation of the c-axis, the lateral position of the pump, as well as the pump's angular distribution. Figures 3.5 (c) and (d) show a front-side and back-side square respectively. As explained above, they are much weaker than the triangle because the two-beam coupling gain falls off rapidly with pump-signal angle. We have observed squares in isolation but they were too weak to photograph well. Many patterns can be excited simultaneously under certain conditions. Close inspection of Figure 3.5 (e) reveals a triangle, a square, and a pentagon. For higher angular distribution of the pump, the triangles tend to get blurred, i.e., they also acquire a high angular distribution, as shown in figures 3.5 (c) and (f). Higher order modes are weaker and tend to be difficult to observe both because they experience less gain as the order grows and because they are obscured by the spherical curvature of the disk outer surface. Hexagons were the highest order observed and multiple patterns such as David stars (two interlaced triangles) were also observed.

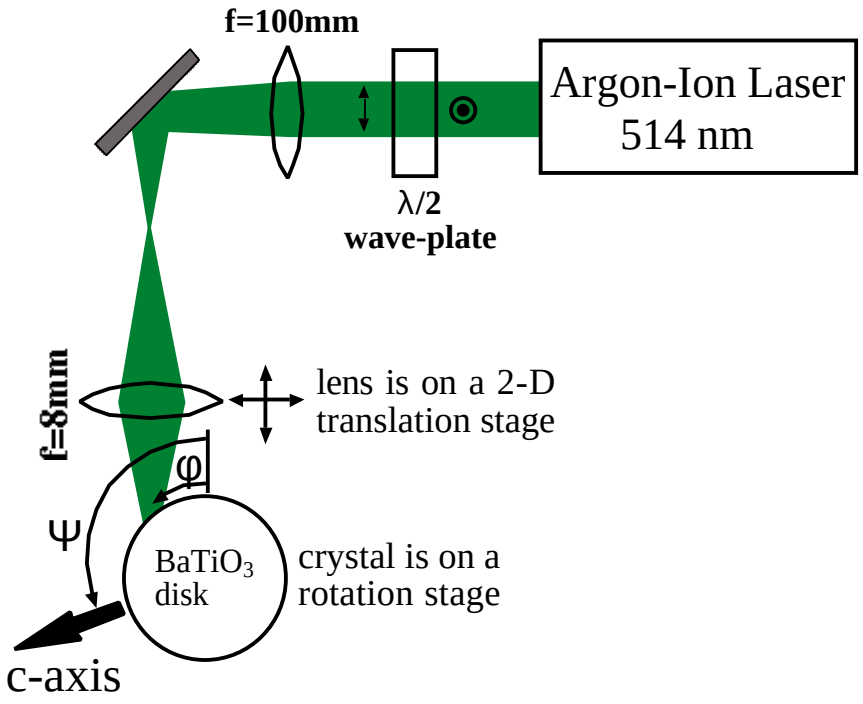

Figure 3.4. Experimental setup for observing oscillating patterns. The angular displacement of the pump is given by φand the rotation of the c-axis by ψNote that the parameters φ and ψ are measured with respect to the vertical line (parallel to the pump) which crosses the center of the crystal.

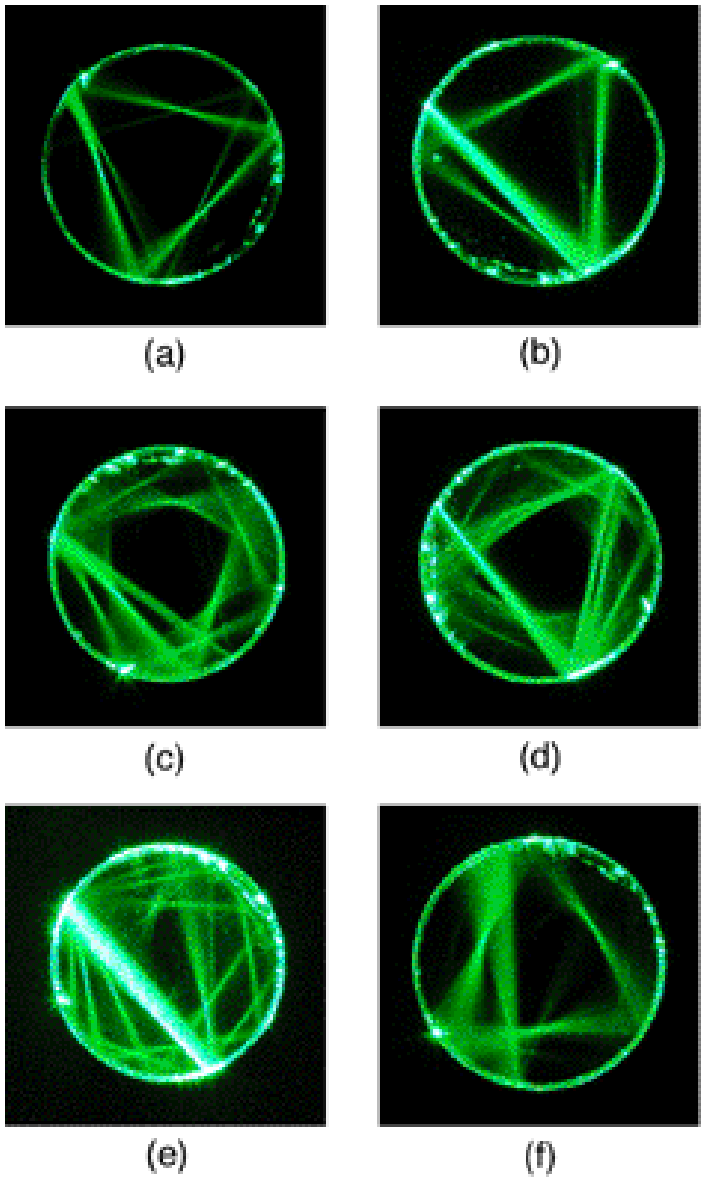

Figure 3.5. Oscillation patterns inside a barium titanate spherical disk.

3.4.2. A theory for the triangle occurrence regions

As further investigation we calculate the gain maxima for triangle excitation using a simple model which uses two-beam coupling of the pump with one side of the triangle. The calculations assume plane-waves for the interacting beams. Specifically, we calculate the c-axis orientation which maximizes the gain for the triangle as a function of the incoming pump-beam angle. Figures 3.6 (a) and (b) show the geometrical relations used in our calculations for a front-side and a back-side triangle respectively. For an input displacement of the pump, given by $r\sin(\varphi)$, the minimum interbeam angle is given by $2\theta=30^{\circ}-\varphi'$, where φ' is the refraction angle with respect to the surface's normal. The two-beam coupling gain curve, given by the expression (see chapter 1, section 1.2)

$$\gamma = \frac{2\pi}{n\lambda\cos\theta} r_{eff}, \quad \text{where} \quad r_{eff} = -2\, n_o^2 n_e^2\, r_{42}\, E_{sc}(\theta,\varphi)\cos\alpha\, \sin(2\varphi), \qquad [3.1]$$

has two maxima when plotted as a function of the c-axis orientation ϕ for a fixed interbeam half-angle θ. Therefore, for each value of the interbeam angle 2θ above we can find from the gain curve two c–axis orientations, ϕ_d and ϕ_r, corresponding to the two maxima. The angles ϕ_d and ϕ_r give the direction of the crystal axis with respect to the bisector of the two interacting beams. The subscript in ϕ_d stands for "direct" denoting that the c-axis direction is less than 90° apart from the bisector, whereas ϕ_r stands for "reverse", and has a value between 90° and 180°. To compare our results to

the measurements, we must reference the direct and reverse c-axis angles to the direction of the incoming pump (the vertical in figure 3.6) thereby obtaining ψ_d and ψ_r. Taking both front-side and back-side configurations in figure 3.6 into account, we end up with four optimum c-axis orientations, yielding four theoretical curves of ψ as a function of the input pump-beam angle φ.

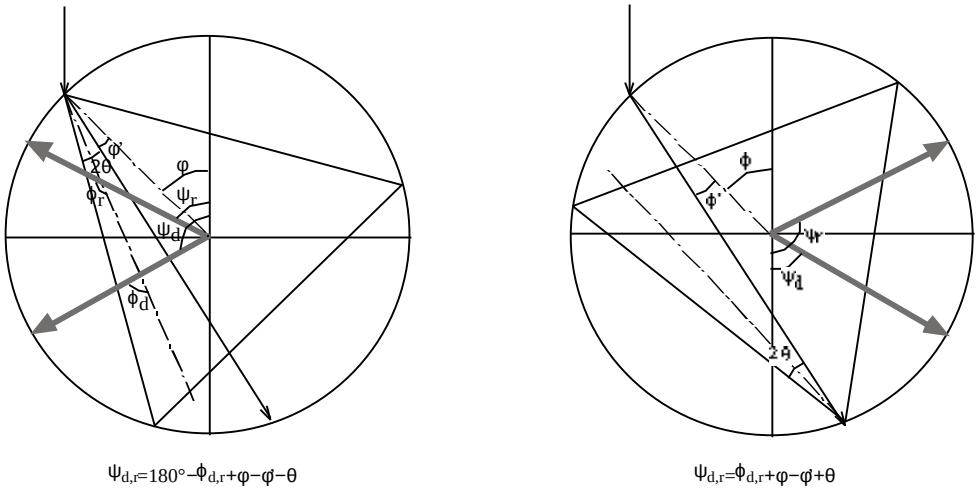

$\psi_{d,r}=180°-\phi_{d,r}+\varphi-\varphi'-\theta$ $\psi_{d,r}=\phi_{d,r}+\varphi-\varphi'+\theta$

(a) (b)

Figure 3.6. Schematic showing the geometrical relationship between ψ and φ for a (a) front-side and (b) back-side triangle. For a given θ, there are two optimum values of ϕ that maximizes the two-beam coupling gain, resulting in also two optimum values of ψ, namely ψ_d and ψ_r.

Figure 3.7 shows the occurrence map for triangles with respect to the incident pump-beam angle (φ) and the orientation of the crystal axis (ψ). Both angles are

referenced to the line that crosses the center of the disk and is parallel to the external incident pump. The four above-mentioned calculated curves (thin lines), corresponding to the theoretical gain maxima, are superimposed over the measured triangle regions (thick horizontal lines). The triangle structures occur over a wide variety of beam parameters. Figure 3.7 shows a reasonable qualitative agreement between the measured regions and the maximum gain calculations. The superposed dotted-lined ellipses are meant to qualitatively indicate the range of parameters over which triangles are observed.

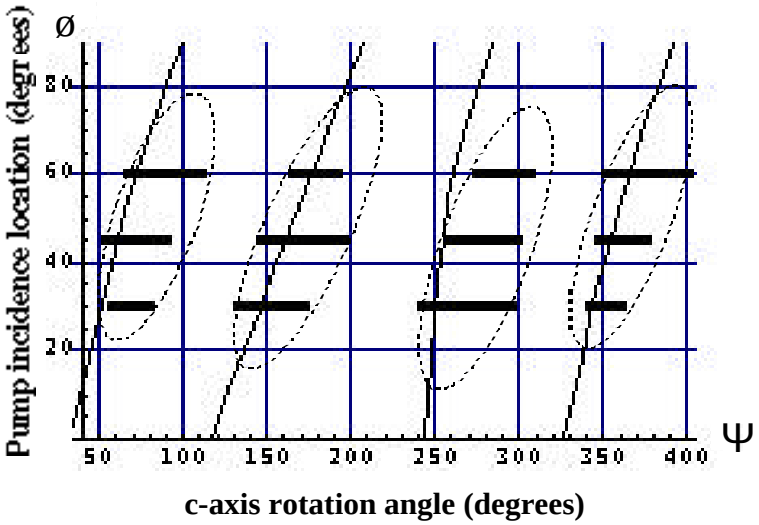

Figure 3.7. Triangle occurrence regions. Dotted ellipses qualitatively show the four regions of the parameter space for which triangles are observed (the pump beam size and divergence are fixed). The horizontal bars show quantitative data regions of triangles. The solid lines represent the four theoretical curves of $\varphi(\psi)$that maximize gain. (The parameter-space coordinates are defined in either figure 3.4 or 3.6.)

3.4.3. Unidirectional oscillation

Two qualitative observations suggest that the oscillating patterns are unidirectional and in the forward direction defined by the pump. First, we observe that the light scattered from nonuniformities in the crystal to be in the forward direction. Second, we never observed a steady phase-conjugate beam. In rectangular-cut crystals self-pumped phase-conjugation of a single pump beam is often observed. [Feinberg,'82] The corners of the crystals act as corner-reflectors that generates the phase-conjugated beam via four-wave mixing. Since the disks and spheres have no corners one might wonder whether self-pumped phase-conjugation can occur. In fact, we were never able to observe steady–state phase-conjugation of the input pump-beam under *any* circumstances in any of our sphere or disk samples. We were able to observe highly unsteady phase-conjugation of the pump beam at normal incidence to the crystal, along the c-axis direction.[1]

3.5. CONCLUSIONS

The spherical barium titanate crystal is interesting for several reasons. Most systems built in our laboratories employ two-beam coupling as a basic function. In many cases, the two-beam coupling unit is used to pump a ring oscillator, such as the case of the auto-tuning filter, which we discussed in the previous chapter and will

[1] Phase-conjugation observations were done by Dr. Dana Anderson and Dr. Vladimir Shkunov.

revisit in the next chapter. By allowing fiber-to-fiber two-beam coupling, the spheres contribute in building compact systems. Compactness not only has the advantage of making photorefractive systems portable and light weight, but also of reducing vibrations and increasing robustness, this last due to the decreased number of elements necessary in the system. The WGM patterns, for now, are only a scientific curiosity. However, one can think of them as a very compact ring oscillator inside the crystal itself. To make them useful for real systems one needs find a practical way of coupling some of the oscillation light out of the crystal. That could be done by frustrating one of the reflections of the oscillating pattern [Schiller, '92] and then coupling to an optical fiber.

Finally, the spherical disk geometry with the c-axis in the plane of the disk is convenient for determining two-beam coupling parameters. In particular, the internal beam angles are not restricted as they are in rectangular-cut samples by Snell's law and the beam geometry is practically independent of crystal orientation, though there is some degree of optical asphericity due to crystal birefringence.

CHAPTER 4:

CARRIER SUPPRESSION WITH TWO-BEAM COUPLING

4.1. INTRODUCTION

Optical carrier suppression can be used in applications where one wishes to eliminate the carrier or increase the modulation depth of an optically modulated signal. One well known example is in photonic links, where it is necessary that the signal be highly linear and therefore the optical carrier be very weakly modulated. Thus, to avoid the saturation of components upon detection, and to decrease the shot noise due to the information-free carrier, a carrier suppressor might be required to increase the modulation depth.

Several techniques for carrier suppression have been demonstrated. A conventional and straightforward technique is to bias a Mach-Zehnder modulator around the minimum transmission point, such that the optical carrier destructively interferes at the interferometer's output, leaving only the sideband modulations. [Montgomery, '95] Another very common technique for carrier suppression in fiber-optic links is that of using stimulated Brillouin scattering, where the carrier propagating inside an optical fiber pumps a beam which propagates in the opposite direction. Optical feedback of the generated beam enhances the carrier suppression and, in fact, a record carrier suppression of 55 dB has been reported by using a

“Brillouin-erbium fiber laser” configuration. [Loayssa, '00; Tonda-Goldstein, '00] Our goal in this project is to build a simple photorefractive carrier suppressor, which, as opposed to the techniques mentioned above, is adaptive due to the real-time holographic nature of photorefractive gratings. Carrier suppression is achieved by a two-beam coupling interaction within a photorefractive barium titanate crystal and uses the principles of an optical novelty filter [Anderson, '89; Khoury, '91]. Similar techniques have been used for optical heterodyning [Hamel de Monchenault, '88; Khoury, '93], the logical opposite of the carrier suppression problem.

The application of our carrier suppression system is as part of a higher level system, the “optically-smart antenna array”. This system, schematically shown in figure 4.1, is composed of an RF-front end active antenna array followed by a photorefractive optical circuit that separates the strongest incoming signal from other weaker ones. For demonstration purposes, the current system uses only two antenna elements and two test-sources, therefore requiring a two-channeled carrier suppressor. The main purpose of the carrier suppressor in this system is to remove the correlation between the modulated optical signals, which is mostly due to the optical carrier, so that the next stage, the autotuning filter, can function optimally. The autotuning filter is the same processor as that described in section 2.5 and its goal, as herein, is to extract the principal component from the various signals presented at its input. Different versions of the auto-tuning filter, some with fiber optics and spherical disks like the ones described in the previous chapter, and others with Gaussian beam optics and other crystal cuts have been tested. However, their use doesn’t pertain to the carrier suppressor and will not be considered further here.

This chapter is divided into three further sections. In the next section we give the theoretical background and introduce a geometrical picture to the "operator formalism", an original theory for describing two-beam coupling interactions. This theory proves to be very useful and, in fact, has played a crucial role in the understanding and, thus, in the development of the carrier suppressor. The goal of the next section is not to formally present the complete operator formalism, which will be treated later in the last chapter, but to give a simplified, geometrical view of this theory. It offers an intuitive understanding of two-beam coupling, and thereby, of the carrier suppression process. It provided us the tools necessary to appropriately set the parameters of the system, such as the modulation index or the input beam ratio of the two-beam coupling interaction.

After several iterations of carrier suppressors, and with the help of the operator theory, a system was built which provided a carrier suppression of more than 70 dB, to our knowledge the best published results so far. Section 4.3 describe the experimental setup and results of this system. We compare the results to the theory presented in the section 4.2 by curve-fitting parameters, such as the input intensity ratio, the gain and the input carrier intensity.

Finally, we close the chapter with a discussion of future work and the issues involved in integrating the carrier suppressor to the above mentioned antenna array application. We first discuss how the performance of the carrier suppressor described in section 4.3 fulfills the performance specifications for that system. We then introduce a new carrier suppressor which takes advantage of a channelized electrooptic modulator design, discuss it's implementation, and expose an important

limitation, that of cross-talk between the channels. Thus, further research on the channelized design is still in progress.

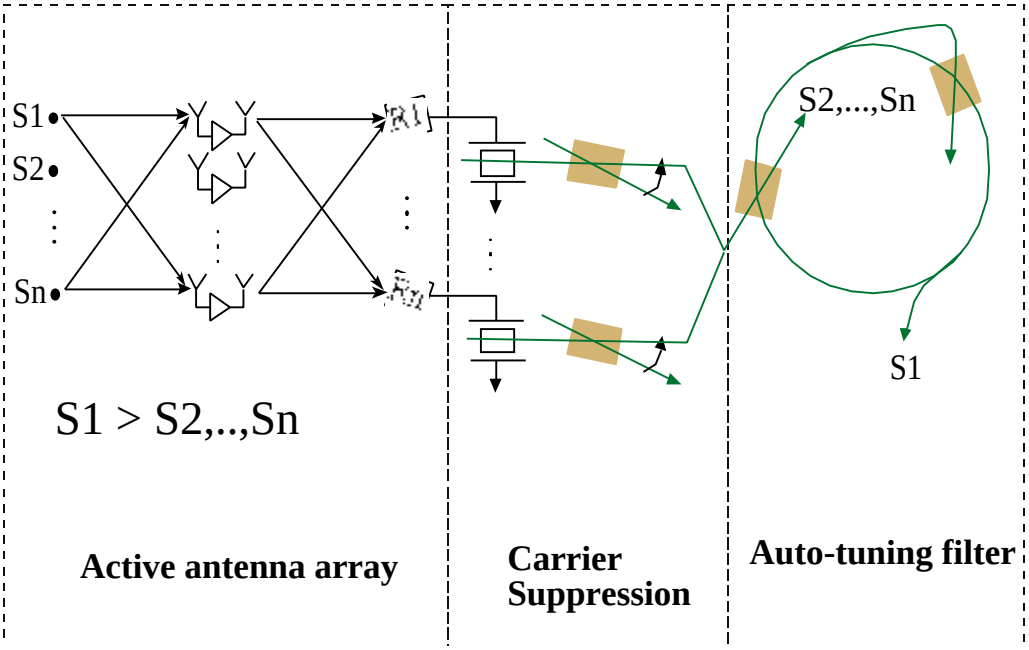

Figure 4.1. Schematic of the optically-smart antenna array, comprising of three parts: the RF front-end which consists of an active antenna array, the carrier suppressor, which consists of electrooptic modulators followed by two-beam coupling in the novelty-filter configuration, and the auto-tuning filter, which consists of a gain crystal pumping a ring with a reflexive-coupling interaction in its feedback path.

4.2. A GEOMETRICAL PICTURE OF TWO-BEAM COUPLING

The current section describes a geometrical picture of the operator theory[1], where the two-beam coupling interaction is viewed as a rotation operator acting on the input fields to produce the output fields. In this simplified exposition of the theory, we assume real coupling, i.e., only pure energy coupling takes place between the beams. With this assumption, the fields can be represented in a two-dimensional space. A geometrical picture of the operator's action over the fields is then constructed. The goal of this section is to provide an intuitive view and understanding of the main aspects of the carrier suppression process. The complete formalism is treated later in chapter 5 and is not necessary in the context of this chapter.

Carrier suppression is schematically shown in figure 4.2. The input to the loss port is the phase-modulated "signal" composed of the optical carrier given by ω_c and the upper and lower sidebands spaced by ω_m from the carrier. The input gain port contains the unmodulated carrier, the "pump". (Note that the definition of signal and pump is opposite than that of previous chapters where the signal beam was the gain port and the pump, the loss port.) In the context of this theory, we refer to the loss port as "minus" port, and to the gain port as "plus". The two beams cross inside the photorefractive crystal where they experience two-beam coupling in the so-called novelty-filter configuration, where any component of the signal that varies faster than

[1] This theory was developed by Dr. Dana Anderson.

the response time of the crystal (τ) will not be able to write a grating and will therefore be transferred to the output minus-port, although some of it will passively scatter to the plus-port due to other gratings that may be present. On the other hand, the components which are slower than τ will write a grating and thereby experience active loss by transferring its energy to the gain port. Thus, when experiencing the two-beam coupling interaction the optical carrier in the signal beam will transfer most of its power to the pump beam whereas the sidebands will scatter only some of its power to the pump beam, therefore resulting in the suppression of the carrier at the output signal port. This process assumes that the modulation frequency (ω_m) is greater than the $1/\tau$, typically 1-100 Hz, depending on the crystal sample. The upper bound for the modulation frequency is given by Bragg matching considerations of the modulated beam to the holographic grating written in the crystal. Two frequencies are considered Bragg matched if the difference in phase that they undergo when crossing the crystal's length l is less then π: $\frac{\omega_1 n}{c} - \frac{\omega_2 n}{c} \leq \frac{\pi}{l}$. This results in an upper bound frequency of a few gigahertz for a 1cm crystal. The energy-transfer process depends on the crystal's gain and the intensity ratio between the two input beams. The gain, in turn, depends on the crystal length and other geometrical parameters.

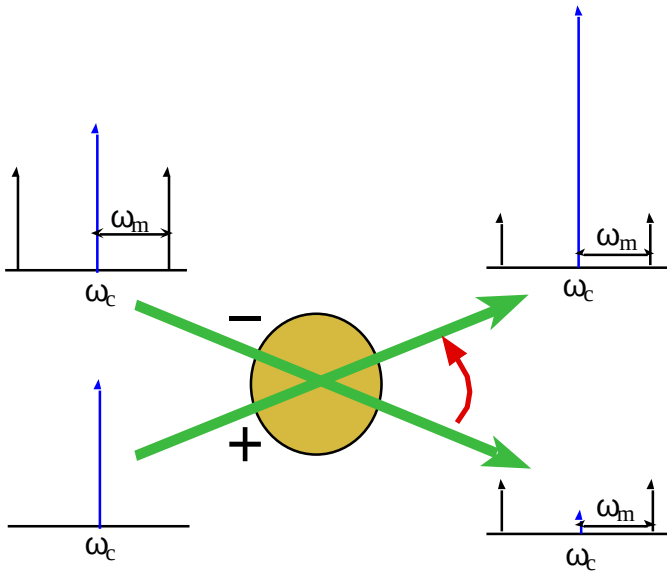

Figure 4.2. Carrier suppression via a two-beam coupling interaction. The input to the minus port is a modulated laser beam while that of the plus port is an unmodulated beam from the same laser. The carrier in the loss port gets transferred to the gain port resulting in a suppressed carrier output.

In the geometrical picture of the operator theory, the different temporal field components of the input signal are represented in a plus-minus coordinate system, defining a "fieldvector"

$$\boldsymbol{E}_{\omega} = \begin{pmatrix} E_{\omega}^{+} \\ E_{\omega}^{-} \end{pmatrix}.$$

To obtain the different components E_{ω}^{+}, the input field at the plus port is decomposed into an orthogonal temporal basis, for instance that of harmonic frequencies, and each component or frequency is labeled by the index ω. Similarly for the temporal field components in the minus port, E_{ω}^{-}.

Assuming real coupling, the fieldvector can then be represented in a plane as shown in figure 4.3. Figure 4.3 (a) shows the vectors corresponding to the fields at the input of the system. The carrier frequency is present at both input ports, plus and minus, and therefore is represented by a "carrier" vector $\boldsymbol{E}_c$, which lies somewhere in the middle of the plane; whereas, since the sidebands are only present in the minus port, they are all aligned with the minus-axis, and can therefore be summed into one single "sideband" vector $\boldsymbol{E}_m$ representing all the sidebands. As we show in the following, a principal eigenvector $\boldsymbol{e}$ can be defined to represent the fields. We also show that the evolution of the system as the fields propagate in the *z* direction through the crystal, is then represented by a rotation of the eigenvector together with all the corresponding fieldvectors, such that the eigenvector asymptotically approaches the plus-axis. This evolution can thus be represented by a single equation for $\phi(z)$, the angle of the principal eigenvector with respect to the minus-axis. The angle of the carrier vector is labeled $\phi_c(z)$.

The mixing between the fields in the two ports can be conveniently expressed by defining the density matrix

$$\rho = \frac{1}{I}\sum_{\omega} E_{\omega}\, E_{\omega}^{\dagger}, \qquad [4.1]$$

where $I=|\boldsymbol{E}_c|^2+|\boldsymbol{E}_m|^2$ is the total input intensity, ω represents the different frequency components and the dagger represents the vector adjoint. Such representation allows the two-beam coupling interaction to be given by a single equation for $\phi(z)$ [Anderson, 2000 #77]:

$$2\frac{\partial\phi}{\partial z} = (\lambda_1 - \lambda_2)\sin(2\phi), \qquad [4.2]$$

where λ_1 and λ_2 are the eigenvalues of the density matrix ρ. The normalized interaction length z points towards the propagation direction in the crystal and is defined in units of $2/\Gamma$, where Γ is the photorefractive coupling constant, which in this case is real. In other words, z does not just represent the physical crystal length, but the gain experienced by the fields as they propagate through the crystal.

The solution to the above equation is given by

$$\tan\phi(z) = e^{(\lambda_1 - \lambda_2)z}\tan\phi(0), \qquad [4.3]$$

which simply means that the principal eigenvector asymptotically rotates towards the plus-axis as it propagates in z, and that this rotation is "slowed down" by the exponential factor $\lambda_1 - \lambda_2$, where $0 \leq \lambda_1 - \lambda_2 \leq 1$ since ρ is normalized. It is important to note that, since all the fields in the crystal share the same grating, all the vectors rotate together. One can think of the eigenvector $\boldsymbol{e}$ as "pulling" the other vectors, $\boldsymbol{E}_c$ and $\boldsymbol{E}_m$, with it.

The main consequence of this rotation to the carrier suppression is the following: As the principal eigenvector rotates towards the plus-axis, it will go through a configuration, shown in figure 4.3 (b), where the projection of the carrier vector on the minus-axis is zero. This means that, for a gain $z=L$ resulting in that particular rotation, there is no carrier present in the output minus-port, i.e., the carrier is perfectly suppressed. It is interesting to note that if the modulation were "off" then $\boldsymbol{E}_m=0$ and the principal eigenvector $\boldsymbol{e}$ would therefore coincide with $\boldsymbol{E}_c$, such that $\phi=\phi_c$. Thus, $\boldsymbol{E}_c$ would only asymptotically approach the plus-axis, meaning that

perfect carrier suppression could not occur for a finite crystal length. However, due to the presence of the modulation $\boldsymbol{E}_m$, the eigenvector $\boldsymbol{e}$ does not coincide with $\boldsymbol{E}_c$. Thus, as $\boldsymbol{e}$ approaches the plus-axis, it will go through a particular value of z where $\boldsymbol{E}_c$ coincides with the plus-axis, meaning perfect carrier suppression at a finite crystal length. In other words, *it is the presence of the modulation which allows for perfect carrier suppression at finite lengths.* From the geometry of figure 4.3 (b), it is easy to show that the rotation $\phi(L)$ corresponding to perfect carrier suppression is simply given by

$$\phi(L) = \arctan\left[e^{(\lambda_1-\lambda_2)L}\tan\phi(0)\right] = 90^\circ + \phi(0) - \phi_c(0). \qquad [4.4]$$

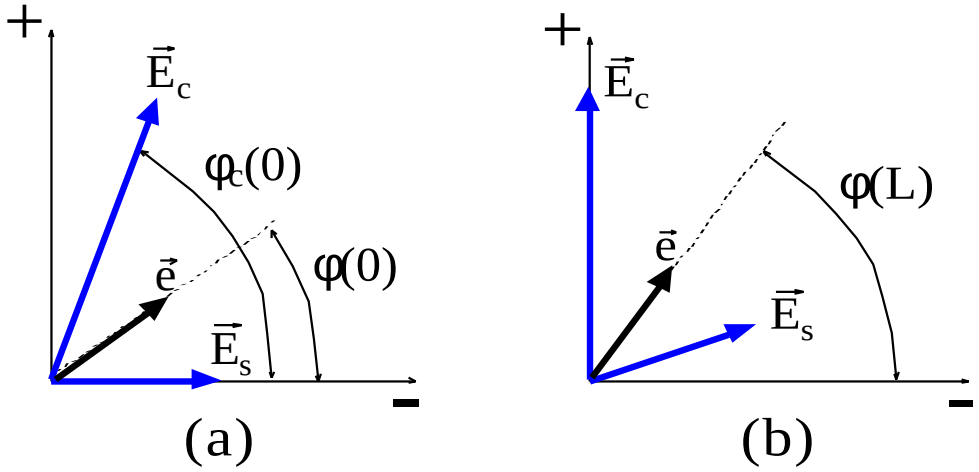

Figure 4.3. Carrier and sideband vectors, $\boldsymbol{E}_c$ and $\boldsymbol{E}_s$ respectively, in the plus-minus coordinate system. The principal eigenvector $\boldsymbol{e}$ embodies the dynamics of the system. (a) Initial position at z=0. (b) Position of vectors after rotation, such that the projection of the carrier into the minus-axis is null, resulting in a carrier suppressed output at that port.

Next, we describe the carrier suppression process by using the following experimentally convenient parameters: r is the intensity ratio between the plus and

minus input ports; and *m* is the modulation strength, defined as the ratio between the power in the sidebands over the power in the carrier at the input minus port:

$$r = \frac{I^{+}(0)}{I^{-}(0)} = \frac{\left|E_c^{+}(0)\right|^2}{\left|E_c^{-}(0)\right|^2 + \left|E_m^{-}(0)\right|^2}; \qquad [4.5]$$

$$m(z) = \frac{I_m^{-}(z)}{I_c^{-}(z)} = \frac{\left|E_m^{-}(z)\right|^2}{\left|E_c^{-}(z)\right|^2}. \qquad [4.6]$$

$E_m^{-}(z)$ and $E_c^{-}(z)$ are the projections of the fieldvectors $\boldsymbol{E}_m(z)$ and $\boldsymbol{E}_c(z)$ into the minus axis after the corresponding rotation of the input fieldvectors by $\phi(z)$-$\phi(0)$, where $\phi(z)$ is given by equation [4.3]. Similarly, $E_m^{+}(z)$ and $E_c^{+}(z)$ are the projections into the plus axis after rotation. At z=0, the modulation strength is given by $m(0)=m_o$. Using equations [4.3], [4.5] and [4.6], the modulation strength, written in terms of r, m_0, and the gain z, is given by

$$m(z) = \frac{m_0}{\left(1 - \sqrt{r(m_0 + 1)}\tan[\phi(z) - \phi(0)]\right)^2}. \qquad [4.7]$$

We discussed above that, for a fixed value of the input modulation strength m_0, there exists a particular gain (z=L) which results in a rotation such that the carrier is perfectly suppressed, i.e. $m(L) \rightarrow \infty$. Conversely, it is also true that, for an arbitrary fixed value of the crystal's gain z, there exists a particular value of m_0 for which the carrier is perfectly suppressed. Figure 4.4 shows four different curves for the modulation strength at the output, $m(z)$, versus that at the input, m_0. Each curve has a peak which goes to infinity. The peak occurs at lower input modulation strength for higher gain and lower input intensity ratio. If the input intensity ratio increases from r=1 to r=9, $m(z)$ is higher everywhere except at the peak of the r=1 curve, however,

that has the cost of reduced light intensity in the signal beam (minus beam). Also, if the gain increases from z=6 to z=12, *m(z)* again becomes higher everywhere except at the peak of the z=6 curve, but now the cost is that the peaks occur for lower m_0.

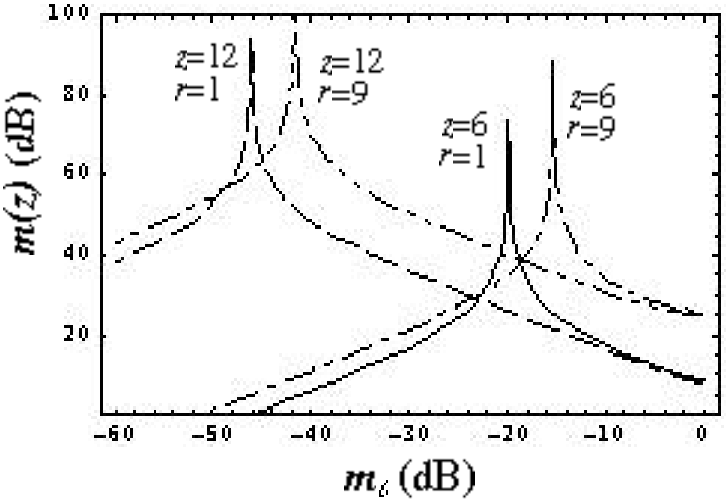

Figure 4.4. Output vs. input modulation strength, for different combinations of gain and input intensity ratio. All peaks go to infinity. Notice that for higher gain the peak occurs for lower input modulation. Except at the peak locations, higher gain or input intensity ratio both result in a general increase of the output modulation, at the cost of decreasing the output signal strength.

In addition, we can find $z=L$ that maximizes *m(z)* by using equation [4.4], where $\phi(0)$ and $\phi_c(0)$ are written as a function of r and m_0:

$$\phi_c = \arctan\left(\sqrt{r(m_0+1)}\right) \qquad [4.8]$$

$$\phi_0 = \arctan\left(\frac{2\sqrt{\frac{r}{m_0+1}}}{1-r+\sqrt{(r+1)^2-4r\left(\frac{m_0}{m_0+1}\right)}}\right) \qquad [4.9]$$

By plotting L as a function of r, as shown in figure 4.5, we find that, regardless of the input modulation strength, perfect carrier suppression requires the least gain at equal input intensity beams (r=1). The above theoretical results are tested in the system discussed in the next section.

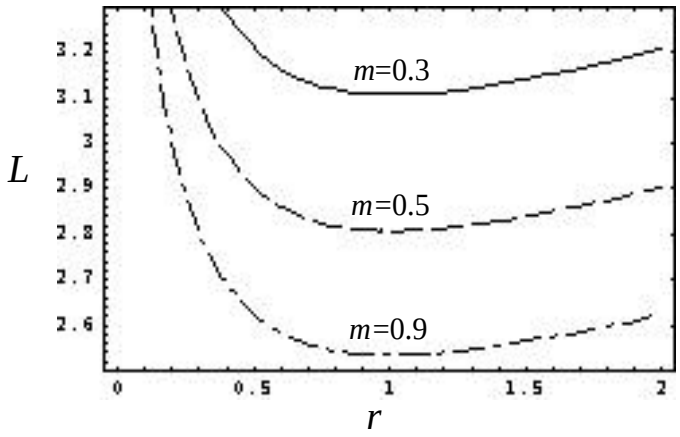

Figure 4.5. Gain required for suppressing the carrier as a function of input intensity ratio for three values of the input modulation strength. Notice that, regardless of the modulation strength, the minimum gain occurs at r=1.

4.3. THE CARRIER-SUPPRESSOR

The operator theory introduced in the previous section provided us with the tools necessary to optimize previous generations of carrier suppressors, and build the photorefractive carrier suppressor described in this section.

We prepare the input signals for the carrier suppressor by modulating the minus port optical beam. For that purpose, we built phase modulators containing lithium niobate crystals doped with magnesium oxide ($MgO:LiNbO_3$). The

magnesium-doped version was selected as it is known to reduce the sensitivity of lithium niobate to optical damage. [Volk, '94] One drawback of the doping is that it causes striations which vary boule to boule, thereby increasing the chance of wavefront distortion as compared to undoped lithium niobate. However, for our application, wavefront distortion doesn't present any problems as the photorefractive grating can correct for it. A $MgO:LiNbO_3$ crystal was tested in our laboratory at 532 nm, the wavelength used in the carrier suppression experiment, and resisted developing significant optical damage below 500 W/cm^2, which for our applications is considered high intensity. Two phase modulators were built, each with a 45.0 x 1.5 x 1.5 mm^3 crystal with a half-wave voltage of approximately 70 V at 532 nm. (The wavelength bandwidth for magnesium-doped lithium niobate is from 500 nm to 900 nm.) The optical transmission of 66% through the modulator is rather low – due both to the uncoated optical surfaces, and to striations inside the crystal which are even visible to the naked eye. Each modulator is driven through a resonant circuit mounted directly on the modulator. The resonant circuit, shown in figure 4.6, is tuned to 129.5 MHz and has a quality factor (Q) of about 15. Including the resonant circuit, the modulator has a modulation efficiency of 0.7 rad/V.

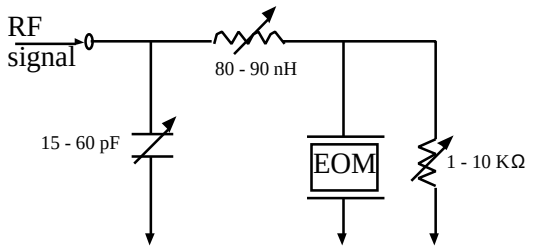

Figure 4.6. Resonant circuit of the electrooptic modulator used in the carrier suppressor.

The carrier suppressor is built with 1" optical height standard, resulting in a compact system of about 38 x 38 cm^2, which reduces the system sensitivity to vibrations and acoustic noise. A picture of the carrier suppressor is shown in figure 4.7 (a). Figure 4.7 (b) shows the setup schematic of the test system. The laser is a doubled Nd:YAG at 532 nm wavelength. A telescope brings the 2.2 mm diameter beam down to about 500 μm. A half-wave plate, followed by a polarizing beam splitter, allows for a variable splitting of the beam. We adjust the splitting intensity ratio so that r=1 at the input of the photorefractive crystal, which, as mentioned in the previous section, minimizes the gain necessary for optimum carrier suppression. One of the beams enters the electrooptic modulator and is modulated by a 129 MHz signal. Since optimum photorefractive interaction occurs with pure-extraordinary input polarization, a polarizer with a 10^{-5} extinction ratio is placed at the output of the modulator to reduce the ordinary polarization component from the signal beam. This beam then crosses the unmodulated beam inside a barium-titanate crystal. A heterodyne detection scheme[1] enabled the direct measurement of the output carrier and modulation sideband strengths. The heterodyne beam is shifted by 80 MHz with respect to the optical carrier via an acoustooptic modulator.

[1] Suggested by Bruce Tiemann.

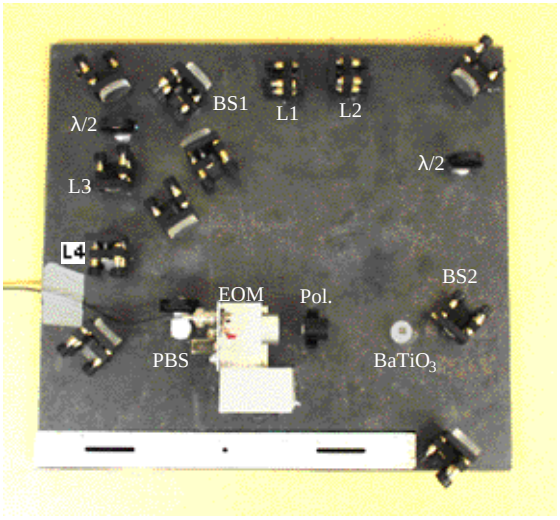

(a)

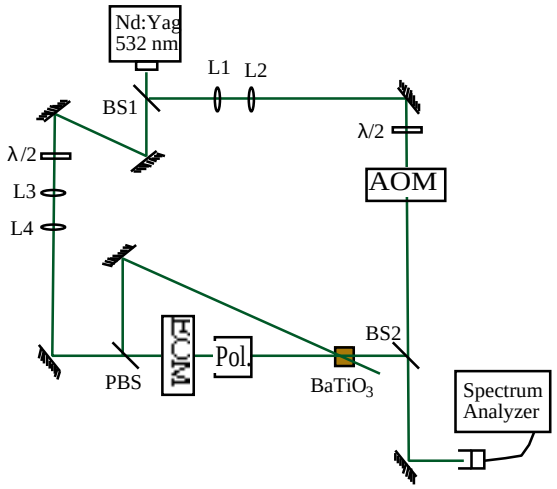

(b)

Figure 4.7. (a)Picture and (b)Setup of the carrier suppressor. (At the time the picture was taken the acoustooptic modulator had been temporarily removed. BS: beam-splitter, PBS: polarizing beam-splitter, L1 and L3: 20 mm focal-length lenses, L2 and L4: 6.15 mm focal-length lenses, EOM: electrooptic modulator, AOM: acoustooptic modulator, λ/2: half-wave plate, Pol.: 10^{-5} extinction-ratio polarizer. All unspecified optics are mirrors.)

To characterize this system we varied the input modulation strength imposed by the modulator and observed the resulting carrier output as displayed by the spectrum analyzer. From a theoretical standpoint, we could have also varied the gain, but this is not as easy to do experimentally in a well-controlled manner. The measured intensity of the carrier at the minus output port (I_c^-) is plotted in figure 4.8 as a function of the modulation index *(*β*)*.[1] A theoretical curve is also shown. We notice two dips of the output carrier strength. The dip at β=2.4 corresponds to a carrier nulling due to the phase modulation process. This zero is not of interest as, first, it is not adaptive and tends to suffer drifts, and second, at this modulation index, the modulation of the signal component is highly nonlinear and has negative slope. Our interest is focused in the first dip occurring at a modulation index of β 0.11, which is due to the photorefractive carrier suppression. The parameters to the theoretical curve are found by least-squares curve-fitting the data to the theory presented in the previous section. Both the theoretical curve and the data are referenced to the value of the output carrier power when the suppressor is "off", i.e., except for passive losses, the output beam is a replica of the input beam. However, since this reference could not be reliably measured, we included it as a parameter in the fit, along with the input intensity ratio *r*, and the normalized length *z*. We also assumed a noise floor to avoid numerical instabilities caused by the infinite dips in the fitting function. The noise floor was set at the measured noise floor of the system, –100 dBm as given by the spectrum analyzer. This value was due to a combination of

[1] This particular set of data was taken by Amy Sullivan.

noise in the detection process and leakage of the carrier through the acoustooptic modulator in the heterodyne detection beam. The parameters *r* and *z* were found to be 1.22 and 6.47, with standard errors of 0.16 and 0.04, respectively.

This first dip shows an output carrier suppression of –71.4 dB ± 1.3 dB. The theoretical curve, the data and the noise floor at –76.8 dB is showed with respect to the fitted reference, which is normalized to 0dB. Notice that at the higher data values the fitted function is higher than the data due to systematic errors. Otherwise, there is good qualitative agreement between the theoretical and experimental curves. The average error between the data and fitted function is 3.7 dB.

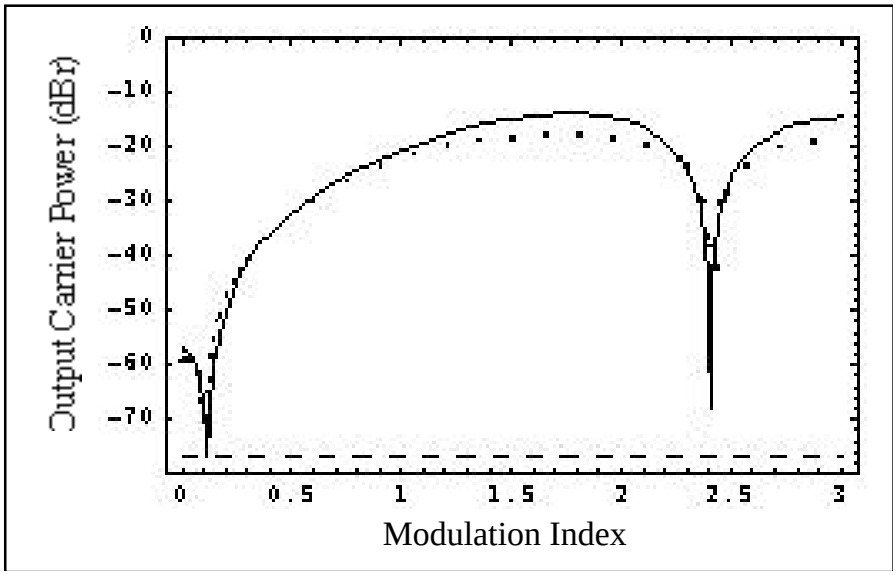

Figure 4.8. Measured output carrier power as a function of modulation index. The output carrier is normalized to the value obtained when the carrier suppression is "off". The first dip of –71.4 dB is due to the photorefractive interaction, whereas the second dip is due to a null of the carrier at the phase modulation process (when β=2.4).

From the curve in figure 4.8 we obtain the curve for the output vs. input modulation strength, which is shown in figure 4.9 (compare to the theoretical plots shown in figure 4.4). This curve results in a peak output modulation strength of about *m(z)*=44 dB.

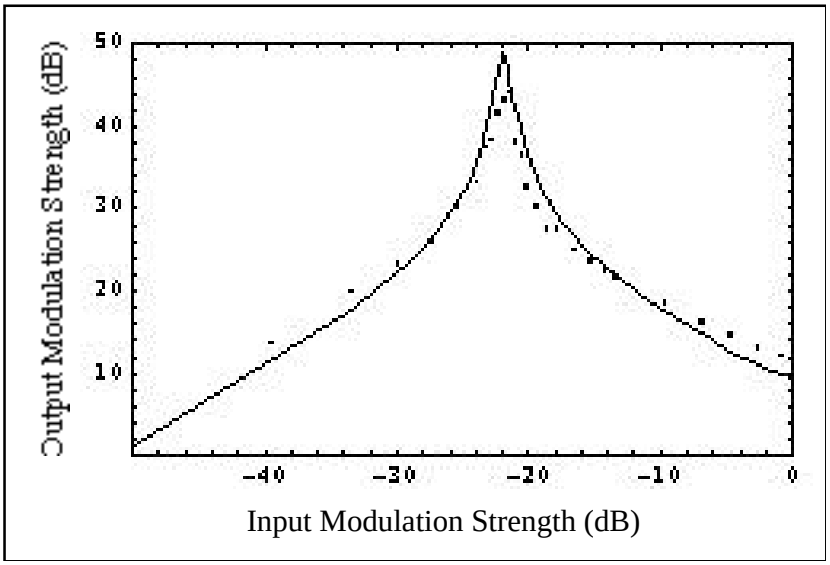

Figure 4.9. Output vs. input modulation strength obtained from fitted carrier suppression data.

As discussed earlier, the original application for the carrier suppressor is as part of the optically-smart antenna array system. The next section discusses how this carrier suppression fulfills, on a per-channel basis, the *performance*-requirements for the antenna array system. However, the antenna array system has *space*-requirements, demanding a re-design of the carrier suppressor to process several channels in a compact space. In that section, we introduce a design that can potentially fulfill these requirements, and discuss its current limitations.

4.4. FUTURE WORK

As described in the introduction to this chapter, the application for our carrier suppressor is as an intermediate stage of the optically-smart antenna array (see figure 4.1), where its function is to provide uncorrelated signals to the following stage, the autotuning filter, by suppressing the carrier. The goal of the work described in this chapter is to demonstrate carrier suppression performance necessary for integration with the antenna array.

A carrier suppression of more than 70 dB was obtained which is above the 30 dB estimated to be necessary at the input of the autotuning filter. Additionally, the signal-to-pump ratio of 1:1 makes the minimum input power for the autotuning filter of 10 mW easily attainable.

After integrating the carrier suppressor with the autotuning filter, the next step is the integration of the optical processor, consisting of both the suppressor and the filter, to the RF front-end. In order to maintain optimum carrier suppression, for a particular gain of the photorefractive crystal, it is necessary that the input modulation strength m_0 be maintained at a specific value which results in a peak of the modulation depth, as discussed in section 4.2. For a variable input RF signal, it becomes necessary to have a mechanism that automatically adjusts the modulation strength to the optimum level. We suggest the use of an automatic gain control amplifier in front of the modulator's driver.

Adequate carrier suppression performance is demonstrated in this chapter, however the incorporation of the carrier suppressor in the antenna array system requires a design that can process several channels in a compact space. The antenna array system's first iteration contains only two channels, but the design should be expandable to more channels for future iterations. In the following, we introduce a double-channeled carrier suppressor design that fulfills these requirements. Such design is still under development as the first implementation attempt ran against some cross-talk problems, as discussed below.

The main difference between this new carrier suppressor and the previous one resides in a new electrooptic modulator design, shown in figure 4.10. This modulator design integrates two modulation channels in the same crystal. The modulator's input laser beam is shaped into a vertical line and the upper and lower portions of the beam are modulated by different signals. The modulated beam then crosses a similarly shaped but unmodulated beam inside the photorefractive crystal, suppressing the carrier from the output beam and thereby revealing the modulation structure of the beam. The channelized modulator design can be expanded to integrate more than two channels without significantly changing the size of the optical system. In fact, using this compact modulator design, we built a 41 x 20 cm^2 double-channel carrier suppressor, more compact than the previous single-channel one, even though they both utilize 1"-optics. Figure 4.11 shows a picture of this system with its corresponding setup.

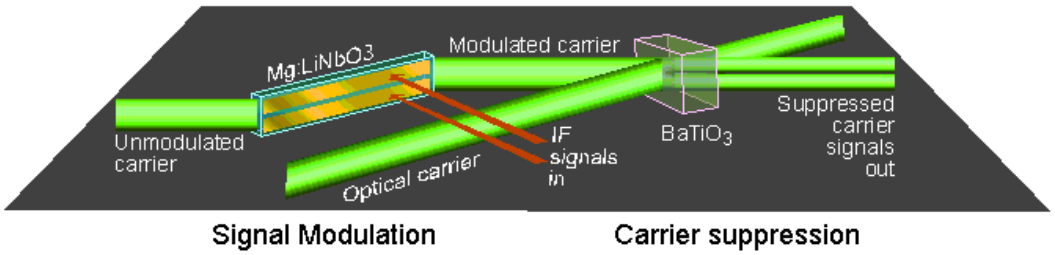

Figure 4.10. Channelized electrooptic modulation and carrier suppression. The modulator imposes spatial and temporal modulation on the optical carrier. The optical carrier is then suppressed by a photorefractive two-beam coupling interaction, revealing the spatial modulation.

The channelized electrooptic modulator contains a thin 0.7 x 5.2 x 45.5 mm^3 slab of magnesium-doped lithium niobate crystal, where the optical facets have been cut at Brewster's angle, about 65°, in order to minimize reflections. The electrodes consist of two copper strips, approximately 2 mm wide and separated by about 1.5 mm. Each electrode is separately fed with a narrow-band matching circuit similar to that used in the modulators in the previous section. The center frequency is set to 105 MHz giving a modulation efficiency of about η=0.4 rad/V.[1]

Other than the channelized electrooptic modulator, there are very few differences between the setup of this system and that of the previous one. To couple light into the electrooptic modulator, a 30° laser line generator lens (from Edmund Scientific Inc.) is used. The heterodyne beam for the output measurement is split directly out of the pump beam. The transmission through the modulator in this setup was about 85%.

[1] Dr. Stefania Romisch collaborated with the modulator's assembly and characterization.

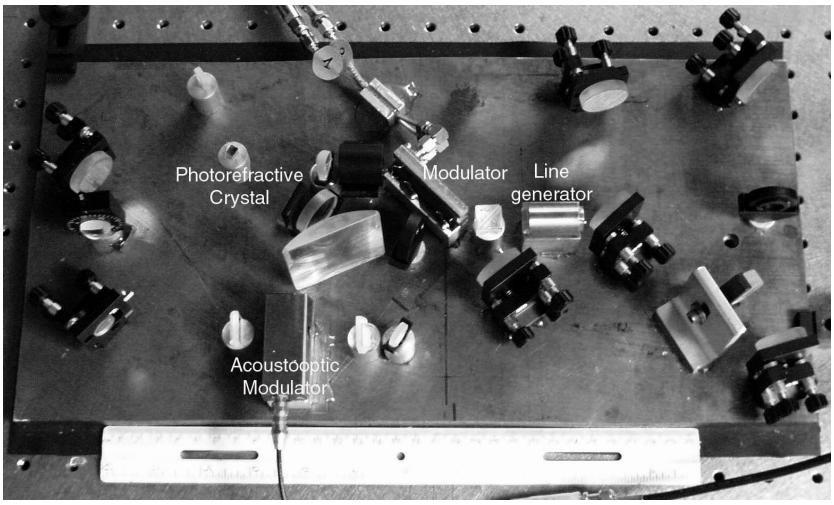

(a)

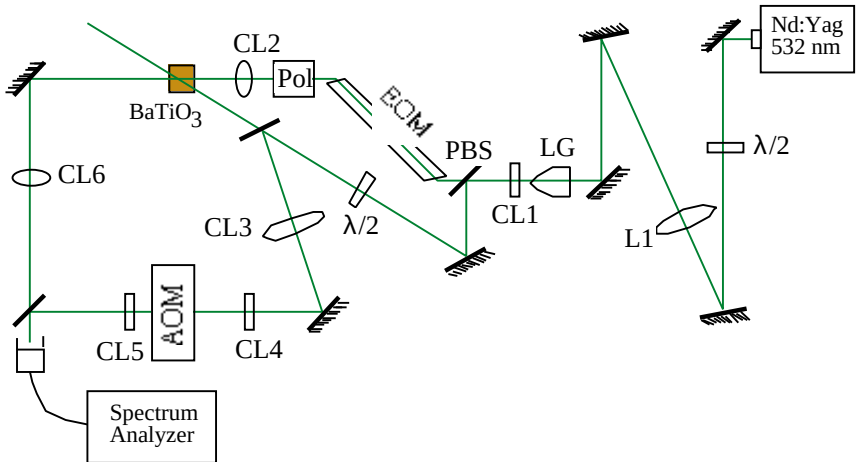

(b)

Figure 4.11. (a) Picture and (b) corresponding setup of carrier suppressor with the channelized electrooptic modulator. (Component abbreviations are the same as those in figure 4.9. Additionally, LG: 30° line generator, CL: cylindrical lenses (CL1: f_y=8 mm, CL2: f_x=30 mm)).

However, when testing this system, we found a severe limitation - that of cross-talk between the two channels. The cross-talk was first revealed by a qualitative, visual method: by using the photorefractive crystal to suppress the carrier, we drive each channel, one at a time, and visually check how the signal beams overlap at the output. We found a significant overlap. To quantify this overlap, we measured the beam directly at the output of the modulator. The data in figure 4.12 shows the intensity of the signal component, the carrier, and second order sideband, as seen by the spectrum analyzer. The measurements were made by moving the photodiode detector along the beam line and optimizing the alignment of the heterodyne detection at each point. The modulator was driven at 105 MHz with 25 dBm. In channel 2 the modulation index achieved higher values (going past the dip at β=2.4) than that in channel 1. We find a significant cross-talk between the two channels with the signal from channel 1 extending significantly over the other channel's side, resulting in a cross-talk of about –10 dB. By changing the coupling alignment into the modulator crystal, we could vary which channel displayed the worst coupling into the other channel's spatial domain, and even adjust for a symmetric coupling, however, the cross-talk remains.

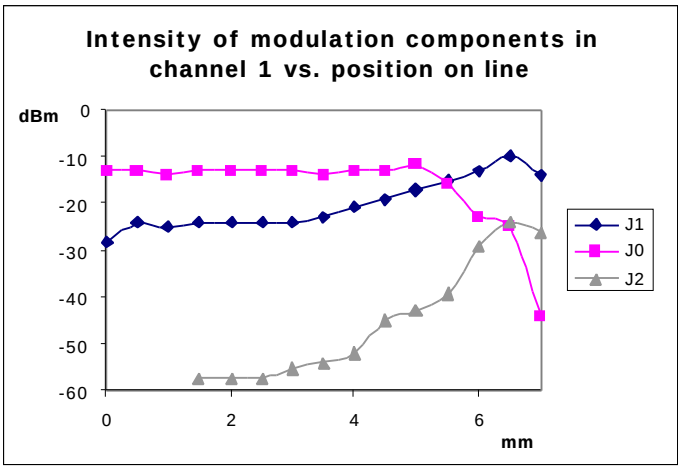

(a)

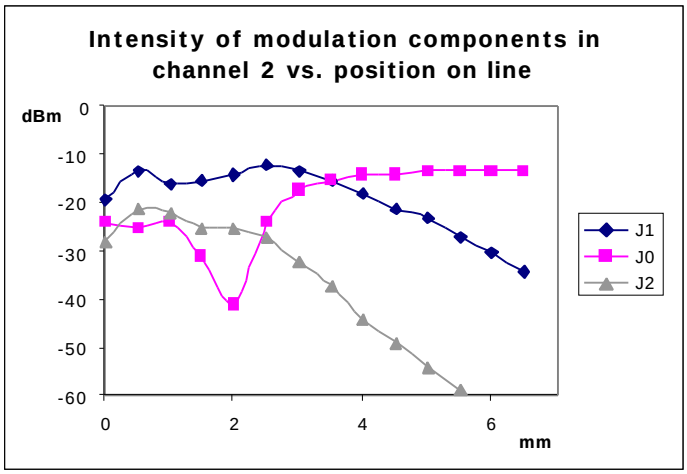

(b)

Figure 4.12. Output intensity of the carrier (J_0), signal (J_1) and second order component (J_2) on (a) channel 1 and (b) channel 2. The signal on channel 1 is more weakly modulated and extends into the spatial domain of channel 2.

The origin of the cross-talk is currently a matter of debate. The most likely cause is the RF coupling between the resonant circuits that drive the electrooptic

modulator. To attack the cross-talk issue, research in this new system design is still under progress.

Alternatively, one could develop a new design which can potentially process several channels. For instance, we suggest using a grating to generate separate beams which can be made parallel by an adjustable prism system. The beams would then enter separate modulators, which however are mounted on a single block. RF coupling could be reduced by a metal shielding between the driving circuits, while optical coupling would be eliminated by the air space between the modulating crystals.

CHAPTER 5:

AN OPERATOR APPROACH TO TWO-BEAM COUPLING:

THE 2-BY-2 COMPLEX-COUPLING CASE

5.1. INTRODUCTION

In this chapter we present an operator theory for describing the process of two-beam coupling. This photorefractive interaction is represented by a black box which operates over the input optical fields to produce the output fields. The input and output fields are represented by vectors, the "fieldvectors", and the black box transformation by the coupling operator T:

$$E_{out} = T\, E_{in} \ . \qquad [5.1]$$

The operator theory is based on the same underlying physics as the standard approach for two-beam coupling. [Kukhtarev, '79] However, the nature of operators confers to this theory its main advantage over the standard approach: a mathematical notation that can deal with complicated spatial modes. This lends the power of representing the information as is the most convenient for the information processing application in hand. For example, if the input optical signals are faces, in the standard approach the faces are decomposed into a superposition of plane-waves, and a

differential equation would result for each pair of plane waves, resulting in a complicated problem. With the operator theory the spatial basis may be chosen to be a set of orthogonal facial features, bridging the gap between the mathematical notation and the information processing task at hand.

Because the operator theory is based on the same physical model as the standard approach, it shares the same limitations and approximations. In particular, this theory assumes steady-state gratings, in other words, the spatial and temporal variations of the fields must be such that the gratings reach a stationary state. This means that the temporal components should vary fast enough such that a component in one beam only writes a grating with the corresponding component in the other beam, and with no other. At the other end, the temporal variations should not vary as fast as to cause the Bragg degeneracy between different optical frequencies to be broken. As mentioned earlier in this thesis, for barium titanate, these conditions limit the frequency components to lie between about hundreds of hertz and a few gigahertz for a 1cm crystal. This theory also assumes that the different spatial components are Bragg distinct, in which case we can think of each spatial component as having its own independent grating. Finally, the operator theory assumes that the coupling between the beams in each port are all described by the same coupling constant Γ. This coupling constant is in general complex, meaning that both energy or phase exchange may occur between the coupled beams. [Yeh, '93]

$$\Gamma = |\Gamma| e^{i\gamma}. \qquad [5.2]$$

The fieldvectors in equation [5.1] has two components, E_+ and E_-, corresponding respectively to the gain and loss port of the two-beam coupling interaction. In their turn E_+ and E_- can be decomposed into their various spatial modes. In general, the number of orthogonal spatial modes at the gain port, *p*, may be different of that in the loss port, *m*.

$$E = \begin{pmatrix} E_+ \\ E_- \end{pmatrix} = \begin{pmatrix} E_{+,1} \\ \vdots \\ E_{+,p} \\ E_{-,1} \\ \vdots \\ E_{-,m} \end{pmatrix} \qquad [5.3]$$

The operator theory for the general case of $p+m$ spatial modes can be solved numerically and are treated in [Anderson, '00; Anderson, '99], and its details will not be covered in this chapter. Our interest is in the simple case of $p=m=1$, meaning that there is a single spatial component in each port, resulting in a 2x2 dimensionality for the coupling matrix *T*. For this "2-by-2 case", there exists closed-form solutions for the two-beam coupling evolution and the coupling matrix *T*.

This chapter follows with three sections. Section 5.2 introduces the general operator formalism.[1] Section 5.3 treats the 2-by-2 case with complex coupling culminating with the solution of *T* for this case. We also present the special cases of purely real and purely imaginary coupling.

[1] The general theory was developed by Dr. Dana Anderson.

Back in chapter 4, section 4.4, we presented a simplified geometrical picture of the operator approach for the 2-by-2 case, assuming purely real coupling and real input fields. Although the current chapter stands alone, the simplified picture presented in chapter 4 may help lend a preliminary intuitive understanding of the operator algebra. Other approaches using an operator or matrix formulation for two-beam coupling are given in[Liu, '93; Ringhofer, '00; Stojkov, '92].

5.2. THE OPERATOR FORMULATION

Given spatially and temporally varying beams as the input to the two-beam coupling, the fields can be decomposed into a spatial basis, as shown in equation [5.3], as well as into a temporal basis. We will label the different temporal components of the input beams by the subscript ω, but it is understood that these components are not necessarily harmonic components, but any orthogonal temporal basis. The evolution of each temporal component as it propagates through the crystal is given by equation [5.1], rewritten here as

$$E_{\omega}(z) = T(z)\,E_{\omega}(0)\,, \qquad [5.4]$$

where *z*, the interaction length in the direction of propagation, is measured in units of $1/|\Gamma|$,where $|\Gamma|$ is the coupling constant modulus, so the only part of the coupling constant that appears in our equations is it's phase factor γ as defined in equation

[5.2]. The field values at any position z within the crystal is determined by solving for the coupling operator T. As we will see later, T corresponds to a rotation operator which conserves the length of the fieldvectors (meaning that the transformation is lossless) and is therefore Unitary, i.e. $T^{\dagger} = T^{-1}$. The formulation involved in solving for T follows.

In an analogy to quantum mechanics, we introduce a "Hamiltonian" H, a transformation that determines the evolution of the fieldvector such that

$$E'(z) = -iH(z)\,E(z), \qquad [5.5]$$

where the prime denotes derivation with respect to z. The Hamiltonian operator represents the effect of the grating on the evolution of the fields in each location z. It will later be defined such as to embody the two-beam coupling physics in the context of our operator formulation, but because the grating itself is formed by the fields, we can anticipate that H(z) will depend on the fieldvectors. However, this fact does not affect the validity of equation [5.5].

The black-box view, given by the coupling operator T, and the above fieldvector evolution, given by H, can be connected by simply substituting equation [5.4] in the above equation, giving

$$T'(z)E_{\omega}(0) = -iH(z)T(z)E_{\omega}(0), \qquad [5.6]$$

which, by eliminating $E_\omega(0)$, gives us a differential equation for the coupling operator:

$$T' = -iH\ T, \qquad [5.7]$$

where the explicit *z*-dependence is dropped.

Our problem involves the mixing between two input beams or ports, which translates into a mixing of the components of the fieldvector. Thus a "density operator", ρ, which represents the mixing between the components is introduced:

$$\rho = \frac{1}{I}\sum_\omega E_\omega \times E_\omega^\dagger , \qquad [5.8]$$

where $E_\omega^\dagger$ is the adjoint (complex-transpose) of E_ω, and I is the total intensity:

$$I = \sum_\omega I_\omega = \sum_\omega E_\omega^\dagger E_\omega \ .$$

In the 2-by-2 case, the density operator in the gain and loss port space is given by the density matrix:

$$\rho = \frac{1}{I}\sum_\omega \begin{pmatrix} \left|E_{\omega,+}\right|^2 & E_{\omega,+}E_{\omega,-}^* \\ E_{\omega,+}^* E_{\omega,-} & \left|E_{\omega,-}\right|^2 \end{pmatrix} \qquad [5.9]$$

Characterizing the system by the density operator is equivalent to characterizing it by its fieldvectors, with the advantage that it simplifies and suits the problem. [Cohen-Tannoudji, '77b] The density operator is Hermitian, and, because it is normalized, it has a unity trace:

$$Tr(\rho) = \sum_i \rho_{ii} = 1.$$

Just as we had represented the fieldvector in the black-box view of equation [5.4], we can equivalently represent the density matrix at some location *z* as a function of the input density matrix by simply substituting equation [5.4] in equation [5.8], obtaining

$$\rho = T\rho(0)T^{\dagger}. \qquad [5.10]$$

And, again, equivalently to equation [5.5] for the fieldvectors, we can write a differential equation for the density operator, which is obtained by combining the above equation [5.10] with equation [5.7], giving

$$\rho' = -iHT\rho(0)T^{\dagger} + i\,T\rho(0)T^{\dagger}H = -i[H,\rho], \qquad [5.11]$$

where $[A,B] = AB - BA$ is the "commutator" of *A* and *B*.

The equations above hold independently of the physics of the problem. As mentioned above the physics is included by defining an appropriate Hamiltonian,

which satisfies the assumptions and approximations of the physical model described in the introduction of this chapter. It is given by

$$H = \frac{i}{4} e^{i\gamma\sigma_3} \left[\sigma_3, \rho\right], \qquad [5.12]$$

where ρ is the same density operator defined above and σ_3 is an operator which embodies the asymmetry of the coupling mechanism, and, in the 2-by-2 representation, is given by the Pauli spin matrix

$$\sigma_3 = \begin{pmatrix} 1 & 0 \\ 0 & -1 \end{pmatrix}.$$

The factor of *i* in the Hamiltonian makes it Hermitian. This two-beam coupling Hamiltonian is not derived here from first principles, but, upon substitution in equation [5.11], the resulting equations for the 2-by-2 case can be shown to reduce to that of the standard approach. [Anderson, '00]

5.3. A CLOSED-FORM SOLUTION TO THE 2-BY-2 CASE.

The operators defined in the previous section are valid in the general case, when a superposition of spatial modes are present in each beam (the n-by-n case). We now focus on the 2-by-2 case where only one spatial mode is present in each beam.

For this simple case, closed-form solutions exist for both the density operator ρ and the coupling operator *T*. From this point forward, we will cease to refer to them as operators but instead refer to their 2-by-2 matrix representation.

Any 2-by-2 matrix can be represented by a superposition of the unit matrix and the Pauli spin matrices. As we progress on the problem of deriving the coupling matrix, we will see that such a representation proves to be very well suited for the density matrix [Cohen-Tannoudji, '77a]:

$$\rho = \frac{1}{2} + \sum_{i=1}^{3} s_i \sigma_i , \qquad [5.13]$$

where

$$\sigma_1 = \begin{pmatrix} 0 & 1 \\ 1 & 0 \end{pmatrix}, \quad \sigma_2 = \begin{pmatrix} 0 & -i \\ i & 0 \end{pmatrix}, \quad \text{and} \quad \sigma_3 = \begin{pmatrix} 1 & 0 \\ 0 & -1 \end{pmatrix}$$

and

$$s_i = \frac{1}{2} Tr(\rho \sigma_i). \qquad [5.14]$$

The Pauli spin matrices have several interesting properties. First, they are idempotent, meaning that $\sigma_i^2 = 1$. Thus $e^{i a \sigma_i} = \cos a + i \sigma_i \sin a$, where *a* is a scalar. Second, they are cyclic upon multiplication, i.e., $\sigma_i \sigma_j = i \varepsilon_{ijk} \sigma_k$ where $i \neq j \neq k$ and ε_{ijk} is 1 for an even

permutation of *i,j,k* and –1 for an odd permutation. Third, they anti-commute, meaning that $\{\sigma_i,\sigma_j\} = \sigma_i\sigma_j + \sigma_j\sigma_i = 0$ where $i \neq j$.

The coefficients of the spin matrices can be conveniently expressed in spherical coordinates:

$$\begin{aligned} s_1 &= \Lambda \sin(2\theta)\cos(2\phi) \\ s_2 &= \Lambda \sin(2\theta)\sin(2\phi) \\ s_3 &= \Lambda \cos(2\theta) \end{aligned} \qquad [5.15]$$

where $\Lambda = \sqrt{s_1^2 + s_2^2 + s_3^2} = (\lambda_1 - \lambda_2)/2$ where λ_1 and λ_2 are the eigenvalues of ρ, with $\lambda_1 > \lambda_2$. The ρ-matrix in the spherical coordinates is simply given by:

$$\rho = \begin{pmatrix} \frac{1}{2} + \Lambda\cos(2\theta) & \Lambda\sin(2\theta)e^{-i2\phi} \\ \Lambda\sin(2\theta)e^{i2\phi} & \frac{1}{2} - \Lambda\cos(2\theta) \end{pmatrix}. \qquad [5.16]$$

We prefer to write the solution of the density matrix and coupling matrix in terms of the spin matrices:

$$\begin{aligned} \sigma_{//} &= \sigma_1\cos(2\phi) + \sigma_2\sin(2\phi) = \begin{pmatrix} 0 & e^{-i2\phi} \\ e^{i2\phi} & 0 \end{pmatrix} \\ \sigma_{\perp} &= \sigma_2\cos(2\phi) - \sigma_1\sin(2\phi) = i\begin{pmatrix} 0 & -e^{-i2\phi} \\ e^{i2\phi} & 0 \end{pmatrix} \end{aligned} \qquad [5.17]$$

As can be deduced from the expressions above, are orthogonal and are obtained by rotating σ_1 and σ_2 around the σ_3 "axis", such that $\sigma_{//}$ is aligned with the projection of ρ into the $\sigma_1\sigma_2$-plane, as shown in figure 5.1.

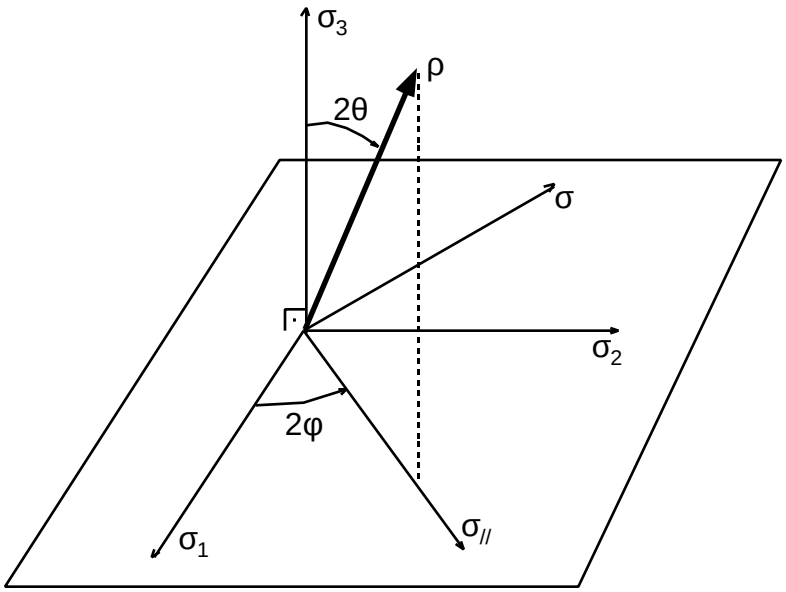

Figure 5.1. Representation of ρ in σ_1 σ_2 σ_3-coordinate space. The "vectors" $\sigma_{//}$ and σ are the parallel and orthogonal projection of ρ on the $\sigma_1\sigma_2$-plane and they rotate in the plane as ρ rotates in space.

Using these, we can rewrite the density matrix as:

$$\rho = \frac{1}{2} + \Lambda\sigma_\rho \qquad [5.18]$$

where

$$\sigma_\rho = \sigma_3 e^{i2\theta\sigma} = \sigma_{//}\sin(2\theta) + \sigma_3\cos(2\theta),$$

points in the direction of ρ.

The expression for the Hamiltonian is obtained by substituting the above ρ in equation [5.12], giving:

$$H = -\frac{\Lambda}{2}\sin(2\theta)\left(\sigma \cos\gamma + \sigma_{//}\sin\gamma\right). \qquad [5.19]$$

Substituting the above H and ρ in equation [5.11], provides the differential equations for θ and ϕ:

$$\begin{aligned} \theta' &= -\frac{\Lambda}{2}\cos\gamma\sin(2\theta) \\ \phi' &= \frac{\Lambda}{2}\sin\gamma\cos(2\theta) \end{aligned} \qquad [5.20]$$

The solution for θ is straightforward:

$$\theta = \arctan\left(e^{-\Lambda z\cos\gamma}\tan\theta_0\right), \qquad [5.21]$$

where $\theta_0=\theta(0)$ and the same convention will be used from this point forward with all variables. Solving ϕ by using $\phi' = \frac{\partial\phi}{\partial\theta}\theta'$, we get

$$\phi = \frac{\tan\gamma}{2}\ln\left(\frac{\sin(2\theta_0)}{\sin(2\theta)}\right) + \phi_0 \qquad [5.22]$$

where

$$\sin(2\theta) = \frac{\sin(2\theta_0)}{e^{\Lambda z\cos\gamma}\cos^2\theta_0 + e^{-\Lambda z\cos\gamma}\sin^2\theta_0}$$

$$\cos(2\theta) = \frac{e^{\Lambda z\cos\gamma}\cos^2\theta_0 - e^{-\Lambda z\cos\gamma}\sin^2\theta_0}{e^{\Lambda z\cos\gamma}\cos^2\theta_0 + e^{-\Lambda z\cos\gamma}\sin^2\theta_0} \qquad [5.23]$$

The solution for ϕ is more usefully casted as:

$$e^{\pm i2\phi} = \left(\frac{\sin(2\theta_0)}{\sin(2\theta)}\right)^{\pm i\tan\gamma} \qquad e^{\pm i2\phi_0} = \left(e^{\Lambda z\cos\gamma}\cos^2\theta_0 + e^{-\Lambda z\cos\gamma}\sin^2\theta_0\right)^{\pm i\tan\gamma} e^{\pm i2\phi_0} \qquad [5.24]$$

With the solution of θ and ϕ at hand, ρ is now solved. The plot in figure 5.2 shows the shape for the evolution of ρ in the $\sigma_1\sigma_2\sigma_3$-space (as shown in figure 5.1) for γ=1.5, i.e., $0<\gamma<\pi/2$. Figure 5.2 (a) shows a view of the south pole, whereas figure 5.2 (b) shows the north pole, which points in the direction of σ_3. Given the initial

conditions θ_0 and ϕ_0, ρ_0 will point to a particular point in the curve and then, as it propagates through the crystal, ρ will follow the curve asymptotically towards the north pole. The value of 2θ is an expression of the intensity ratio between the beams. The north pole corresponds to all the energy being present at the gain port, and the south pole, to it all being present at the loss port. Thus, naturally, the equator corresponds to equal intensities between the two beams. On the other hand, 2ϕ corresponds to the phase-difference between the two beams and the spiraling indicates a phase coupling between the beams. As indicated by the cos(2θ) factor in equation [5.20] for ϕ, the spiraling in the northern hemisphere is in the opposite direction as that in the southern hemisphere. At the equator, no spiraling can occur as the curve is perpendicular to the equator line. This has a simple physical interpretation. Unlike energy transfer, two-beam coupling phase transfer is symmetric, and thus, when the beams have equal intensity they both change their phases at equal rates, resulting in no net change in the phase difference between the two beams.

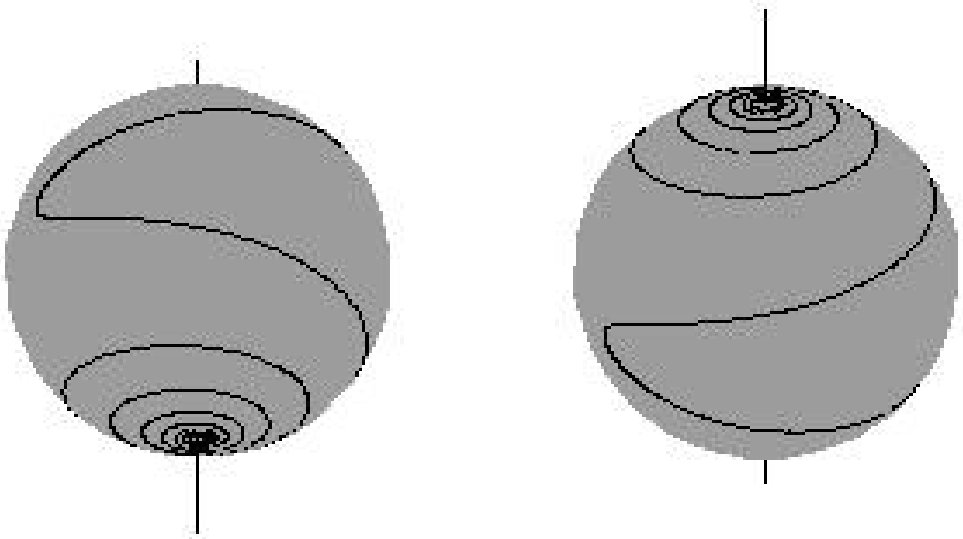

(a) (b)

Figure 5.2. Plot of the evolution of the density matrix ρ as a function of propagation *z* through the medium, for γ=1.5. The initial conditions are θ_0=1.5, close to the south pole (a), where all the energy is in the loss port, and ϕ_0=0. As the density matrix evolves, it spirals up and switches direction at the equator, where θ' is maximum ϕ'=0, and then asymptotically spirals up to the north pole (b).

So, in summary, for the general case of complex coupling, where $0<\gamma<\pi/2$, the energy coupling causes ρ to approach the north pole whereas the phase coupling causes it to rotate around the polar axis σ_3, resulting in the spiral shape shown in figure 5.2. We know from photorefractive physics that a real coupling constant, which occurs for γ=0 (see equation [5.2]), corresponds to pure energy coupling and thus, for this special "real case" we expect the curve to go directly from the south to

the north pole without spiraling. That is indeed the case and is shown in figure 5.3 (a), plotted for $\gamma=0$. Conversely, an imaginary coupling constant, which occurs for $\gamma=\pi/2$, corresponds to pure phase coupling and is represented by a pure rotation around σ_3. We call this the "imaginary case" and it is shown in figure 5.3 (b). Naturally, the longitude of the curve in the real case is given by the constant $\phi=\phi_0$ and similarly, the latitude of the curve in the imaginary case, by θ_0. In the real case the equation for θ is simply given by substituting $\gamma=0$ in equation [5.21]. In the imaginary case, the complex-case expression for ϕ is not valid as it becomes undetermined at that limit. Notice that when $\gamma \to \pi/2$ is plugged in equation [5.22], since $\tan(\gamma) \to \infty$ and $\ln(1) \to 0, \phi$ is undetermined. However, since in this case $\theta=\theta_0$ is constant, the expression for ϕ directly follows from its differential equation [5.20], giving $\phi(z) = \frac{\Delta z}{2}\cos(2\theta_0) + \phi_0$.

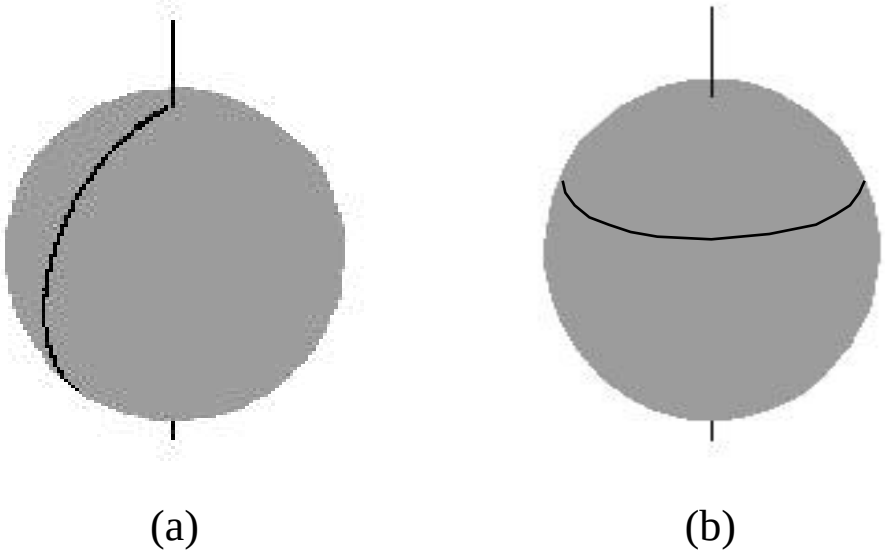

Figure 5.3. Evolution of the density matrix for the special cases of (a) real and (b) imaginary coupling. In the real case of pure energy coupling, ρ follows a longitude line towards the north pole, the longitude being determined by ϕ_0 . In the imaginary case, ρ rotates around the pole with constant speed, the latitude being determined by θ_0.

As described above, the solution to the density matrix provides us with an important tool for understanding the behavior of the system, but our ultimate goal is to solve for the coupling matrix which represents the two-beam coupling black-box. If the chain rule is applied to the differential equation for the coupling matrix, equation [5.7], and the expressions for θ', ϕ', and H (equations [5.20] and [5.19] respectively) are substituted, we get:

$$\frac{\partial T}{\partial \theta}\theta' + \frac{\partial T}{\partial \phi}\phi' + \frac{\partial T}{\partial z} = i\frac{\Lambda}{2}\sin(2\theta)\left(\sigma \cos\gamma + \sigma_{//}\sin\gamma\right)T \qquad [5.25]$$

which has the following solution for T:

$$T = T_\theta\, T_\phi\, T_\rho = e^{-i(\theta-\theta_0)\sigma}\; e^{-i(\phi-\phi_0)\sigma_3}\, e^{i\frac{\Delta z}{2}\sin\gamma\,\sigma_{\rho 0}}. \qquad [5.26]$$

The special limit cases are straightforward by substituting $\phi=\phi_0$ and $\gamma= 0$for the real case, and $\theta=\theta_0$ and $\gamma= \pi/2$for the imaginary case:

$$T_{\mathrm{Re}} = e^{-i(\theta-\theta_0)\sigma} \quad \text{and} \quad T_{\mathrm{Im}} = e^{-i(\phi-\phi_0)\sigma_3}\, e^{i\frac{\Delta z}{2}\sigma_{\rho 0}} = e^{-i\frac{\Delta z}{2}\cos(2\theta_0)\sigma_3}\, e^{i\frac{\Delta z}{2}\sigma_{\rho 0}}.$$

The action of T on ρ is simple: each factor of the type $T = e^{iA\sigma_i}$ corresponds to a rotation of ρ around σ_i by an amount A. So the complex solution in equation [5.26] represents a general rotation of the density matrix decomposed into the following rotations: the first factor to act on ρ, T_ρ, rotates ρ around itself, a degenerate rotation which does not affect ρ; the second factor T_ϕ then rotates ρ around σ_3 by $\phi-\phi_0$; and finally the last term T_θ rotates ρ around σ by $\theta-\theta_0$, which is a rotation directly up towards the north pole (see figure 5.1).

The interpretation of the factors T_ϕ and T_θ are clear, the first represent the relative phase difference between the beams picked up by the phase transfer, whereas

the latter represents the energy coupling. However the interpretation of T_ρ is somewhat subtle. It is interesting to note that if this factor is removed from the solution, the resulting expression still satisfies the relation $\rho = T\rho(0)T^\dagger$ however it will not satisfy the differential equation $T' = -iH\,T$. We believe this is because ρ doesn't have any information about the evolution of the absolute phases of the fields, but only the relative phase between them, so it is indifferent to T_ρ. However, the two-beam coupling equations provide information about how much phase is being transferred from each beam to each other beam, and not only the difference. This information is therefore contained in T by this degenerate-rotation of ρ. For example, we mentioned above that ϕ' is always zero at the equator, however that does not mean that the phase transfer stops at that location, it just means that the phase transfer is symmetrical, and this information is contained in T by T_ρ.

CONCLUSIONS

In this chapter we discuss applications and future work regarding the different aspects of the research presented in this thesis. This thesis revolves around one fundamental photorefractive interaction, the two-beam coupling effect. The contributions described in this thesis are divided into three aspects of photorefractive systems: The first is that of developing a component technology, which includes the demonstration of the two-beam coupling modules described in chapter 2 and by the study of the oscillating patterns occurring inside a barium-titanate spherical disk, in particular the triangle pattern, described in chapter 3. The second is that of building and optimizing a specific photorefractive application, the carrier suppressor, described in chapter 4. Finally, the third is that of developing an analytical tool that can simplify the modeling and prediction of photorefractive systems. In this case, the contribution is the presentation of a general solution for the operator theory in the case of a single spatial mode in each beam, described in chapter 5. These different aspects sometimes overlap. For example, the operator theory provided a model on which to cast the carrier suppression effect, resulting in an understanding of the system which proved to be crucial for its optimization. Below, we give concluding remarks and related applications on the topics covered in this thesis.

The fiber-interconnected two-beam coupling modules are pre-aligned building blocks for photorefractive system design. They provide a way to quickly test an idea without having to invest the time in critical optical alignment which is necessary

when building a conventional system. However, it is important to note that, because the geometry within a module is fixed, they are not well suited for optimization of systems. The utility of the two-beam coupling modules as a component technology was illustrated in the example given in section 2.5, where the inclusion of a reflexive-coupling unit in the autotuning filter's ring provided an increase of the output contrast between two signals which are being separated. It took only a few minutes to include the reflexive-coupling element and test the performance. Future work on the modules should seek to improve their long term stability. In section 2.4 some suggestions for future designs were given, but the main issue to keep in mind in a new design is that the adjustments be external to the final module, thereby reducing the susceptibility to long term alignment drifts. Among the useful applications of the modules, we suggest that of testing different ring configurations. Because the geometry of the modules are fixed, the differences in behavior can then be attributed to the different architectures and not to the geometrical factors of the two-beam coupling configurations. For example, one can compare the behavior of the autotuning filter architecture shown in figure 2.10 (b) with one where the pump crystal is instead located in the reflexive loop (directly in front of the plus input port of the reflexive coupling crystal). Understanding the different rings could result in new ideas for future oscillator-based photorefractive processors.

We believe that our research group is the first to observe the oscillating patterns occurring within a barium-titanate spherical disk. For now, the oscillating patterns observed inside the spherical disks stand mostly as a scientific curiosity, however, in order to devise possible applications for this phenomenon, it is necessary

to first understand it. In fact, the model presented in section 3.4 suggests that the disk patterns are unidirectional miniature oscillators pumped mostly by a single two-beam coupling interaction, and therefore hold the promise for a future integrated ring processor such as the autotuning filter [Anderson, '92].

As part of a system oriented group, it is natural that within the contributions is that of building and optimizing a photorefractive system for a specific processing task, in this case, that of carrier suppression. The carrier suppressor was developed for a specific application as part of a higher level system, where its function is to remove the correlation between temporal signals which are to be discriminated by the next stage, the autotuning filter. Another application for the carrier suppressor demonstrated in chapter 4 would be in laser tuning. In Ye *et al* [Ye, '96] a laser beam, whose frequency is to be tuned, is shifted by an acoustooptic modulator and then locked to a reference cavity. In this case, the reference cavity is locked to the ^{87}Rb D_2 line at 780 nm, however the same concept could be used with the I_2 hyperfine resonances at 532 nm [Jungner, '95]. The carrier suppressor used on such a system would allow the use of electrooptic modulators, therefore providing higher modulation bandwidth and, thus, shorter reference cavities which are typically easier to stabilize. The carrier suppressor described in chapter 4 was the evolved result of several other carrier suppressor predecessors. The earlier systems were not covered by this thesis because, first, they didn't accomplish the specifications of our application, and second, all the important aspects of the carrier suppression physics is covered in the description of the last, optimized system. This system rendered a suppression of more than 70 dB, the highest value reported in the literature [Loayssa,

'00; Tonda-Goldstein, '00]. Despite this successful result, there is room for improvement in other aspects of the system. Section 4.4 provides preliminary results in the implementation of a future carrier suppressor which utilizes a channelized electrooptic modulator design. Although the integration provided by this design is attractive for two or three channels, as the number of channels increases, we believe this design will prove impractical due to crystal size and cross-talk issues. In that case, a possible alternative design is that of using a grating to direct the several beams to independent modulators which are, however, placed next to each other on the same mount.

Finally, in chapter 5, we present a closed-form solution for two-beam coupling for the case of only one spatial component on each port. This solution is cast in terms of an operator algebra which was originally developed by Anderson [Anderson, '00; Anderson, '99] and is summarized in section 5.2. We believe that the solution presented is the most general available in the literature as it includes both complex coupling and any number of temporal components. The work of Saxena *et al* [Saxena, '90] solves the problem of N mutually incohenrent pairs of temporal beams. In this case, they show that complete energy transfer between the two write beams may occur in a finite interaction length, as opposed to the infinite thickness required in the standard case of only one temporal component on each beam. This is the same conclusion we arrived at, for example, in the case of the carrier suppression, where the presence of a sideband allowed for perfect suppression at a finite interaction length. However, their solution includes only the case for real coupling, this is, pure energy transfer. The work from Ringhofer *et al* [Ringhofer, '00] provides the general

complex coupling solution for a phase modulated beam in the gain port, with arbitrary phase modulation strength. However, their solution describes only two temporal components, the carrier and the modulation sidebands, as opposed to an unlimited number of temporal modes as in the solution provided in chapter 5.3. In their paper they also provide an application example, where phase modulation is used in the active stabilization of two-beam coupling by means of an electronically introduced phase feedback. For the case of a single spatial mode on each beam, besides the signal processing applications in our laboratories, such as the demultiplexer [Saffman, '91] or the autotuning filter (previously known as the feature extractor) [Anderson, '92], other applications include RF filtering [Hong, '93], laser bandwidth narrowing [Chomsky, '91] or signal amplification [Hamel de Monchenault, '87]. An application that has currently been brought into the spotlight is that of using heterodyne detection with two-beam coupling for laser ultrasonics [Ing, '91; Puoet, '96; Scruby, '90]. Heterodyne detection with two-beam coupling offers several advantages over the conventional optical heterodyne scheme [Hamel de Monchenault, '88]: First, the signal beam may consist of an arbitrary wave-front, such as speckles for instance, while, in the conventional heterodyne, the signal is limited to a spatial mode which is collinear with the local oscillator plane wave. Second, since the grating adapts to the incident signal wave front, the heterodyne detection is not susceptible to time varying phase distortions which are slow compared to the photorefractive response time. The photorefractive heterodyne detection is well suited for laser ultrasonics, a noncontact method for performing ultrasonic nondestructive evaluation measurements. Unlike the conventional piezoelectric

contact transducers, the noncontact nature of laser ultrasonics allows inspection in high-temperature or otherwise hostile environments. The method typically consists of generation of ultrasound with a high-power pulsed laser followed by detection of the ultrasonic motion of the scattering surface by a photorefractive heterodyne detection setup (see, for example, [Murray, '00]).

In conclusion, this thesis covers important aspects in the development of photorefractive system that utilizes two-beam coupling. It covers, first, the development of component technologies which allow for easy testing of concepts, second, the development of a specific processing system, the carrier suppressor, and finally, it provides a solution for the general case of a single spatial mode two-beam coupling cast in terms of an operator formalism.

BIBLIOGRAPHY

[Anderson, '87]. Anderson, D.Z. and Lininger, D.M., *Dynamic optical interconnects: volume holograms as optical two-port operators*. Appl. Opt., 1987. **26**: p. 5031-8.

[Anderson, '89]. Anderson, D.Z. and Feinberg, J., *Optical novelty filters*. IEEE J. Quantum Electron., 1989. **25**: p. 635-47.

[Anderson, '91]. Anderson, D.Z., *et al.*, *Photorefractive flip-flop*. Opt. Lett., 1991. **16**: p. 250-2.

[Anderson, '92a]. Anderson, D.Z., Benkert, C., and Crouch, D.D., *Competitive and cooperative multimode dynamics in photorefractive ring circuits*, in *Neural Networks for Perception, vol. 2, Computation, Learning, and Architectures*, H. Wechsler, Editor. 1992a, Academic: Boston.

[Anderson, '92b]. Anderson, D.Z., *et al.*, *Optical implementation of a self-organizing feature extractor*, in *Advances in neural-information processing systems IV*, J.E. Moody, S.J. Hanson, and R.P. Lippmann, Editors. 1992b, Morgan Kaufmann: San Mateo, Calif. p. 821-8.

[Anderson, '95]. Anderson, D.Z., Saffman, M., and Hermanns, A., *Manipulating the information carried by an optical beam with reflexive photorefractive beam coupling*. J. Opt. Soc. Am. B, 1995. **12**: p. 117-23.

[Anderson, '99]. Anderson, D.Z., Brockett, R.W., and Nuttall, N., *Information dynamics of photorefractive two-beam coupling*. Phys. Rev. Lett., 1999. **82**(7): p. 1418-21.

[Anderson, '00]. Anderson, D.Z., *A matrix formulation of photorefractive two-beam coupling*. Phys. Rev. A (submitted), 2000.

[Baer, '87]. Baer, T., *Continous-wave laser oscillation in a Nd:Yag sphere*. Opt. Lett., 1987. **12**(6): p. 392-4.

[Baxter, '50]. Baxter, W.T., *Jewelry Gemcutting and Metalcraft*. 3rd ed. 1950, New York: McGraw Hill.

[Breugnot, '95]. Breugnot, S., *et al.*, *Low-noise photorefractive amplification and detection of very weak signal beams*. opt. Lett., 1995. **20**(5): p. 447-9.

[Buse, '97]. Buse, K., *Light-induced charge transport processes in photorefractive crystals. I. Models and experimental methods.* Appl. Phys. B (Lasers and Optics), 1997. **B64**(3): p. 273-91.

[Chang, '90]. Chang, T.Y., Hong, J., and Yeh, P., *Spatial amplification*. Opt. Lett., 1990. **15**(743-745).

[Chomsky, '91]. Chomsky, D., *et al.*, *Laser frequency bandwidth narrowing by photorefractive two-beam coupling*. Opt. Lett., 1991. **17**(7): p. 481-3.

[Cohen-Tannoudji, '77a]. Cohen-Tannoudji, C., Diu, B., and Laloe, F., *Complements AIV and EIV*, in *Quantum Mechanics*. 1977a, Hermann and John Wiley & Sons: Paris, France.

[Cohen-Tannoudji, '77b]. Cohen-Tannoudji, C., Diu, B., and Laloe, F., *Complement EIII*, in *Quantum Mechanics*. 1977b, Hermann and John Wiley & Sons: Paris, France.

[Courtney, '98]. Courtney, D., *et al.*, *Room temperature CW operation of InGaAsP/InP microdisk lasers*. Proc. SPIE – Int. Soc. Opt. Eng., 1998. **3286**: p. 138-51.

[Cronin-Golomb, '84]. Cronin-Golomb, M., *et al.*, *Theory and applications of four-wave mixing in photorefractive media*. IEEE J. Quantum Electron., 1984. **QE-20**(1): p. 12-30.

[Denz, '99]. Denz, C., *Optical Neural Networks*. 1999, FIZ Karlsruhe, Germany: Vieweg; Braunschweig.

[Fainman, '86]. Fainman, Y., Klancnik, E., and Lee, S.H., *Optimal coherent image amplification by two-wave coupling in photorefractive $BaTiO_3$*. Opt. Eng., 1986. **25**: p. 228.

[Feinberg, '80]. Feinberg, J., *Real-time edge enhancement using the photorefractive effect*. Opt. Lett., 1980. **5**: p. 330-2.

[Feinberg, '82]. Feinberg, J., *Self-pumped, continous-wave phase conjugator using internal reflection*. Opt. Lett., 1982. **7**(10): p. 486-8.

[Feinberg, '83]. Feinberg, J., *Optical image processing using four-wave mixing in photorefractive materials*. Proc. SPIE – Int. Soc. Opt. Eng., 1983. **388**: p. 106-11.

[Feinberg, '90]. Feinberg, J., *Phase conjugation with photorefractive materials*. Opt. & Photon. News, 1990. **1**(12): p. 30-3.

[Gabor, '69]. Gabor, D., *Associative holographic memories*. IBM J. Res. Dev., 1969. **13**(156-159).

[Gu, '93]. Gu, C. and Yeh, P., *Photorefractive devices for optical neural networks*. Optical Memory & Neural Networks, 1993. **2**(3): p. 185-98.

[Gunter, '88]. Gunter, P. and Huignard, J.-P., *Photorefractive materials and their applications*. Vol. I & II. 1988, New York: Springer Verlag.

[Hamel de Monchenault, '87]. Hamel de Monchenault, G., Loiseaux, B., and Huignard, J.-P., *Amplification of high bandwidth signals through two-wave mixing in photorefractive $Bi_{12}SiO_{20}$ crystals*. Appl. Phys. Lett., 1987. **50**(25): p. 1794-6.

[Hamel de Monchenault, '88]. Hamel de Monchenault, G. and Huignard, J.-P., *Two-wave mixing with time-modulated signal in $Bi_{12}SiO_{20}$ theory and application to homodyne wave-front detection*. J. Appl. Phys., 1988. **63**(3): p. 624-7.

[He, '94]. He, Q.B. and Yeh, P., *Fanning noise reduction in photorefractive amplifiers using incoherent erasures*. Appl. Opt., 1994. **33**(2): p. 283-7.

[Hong, '90]. Hong, J., Chiou, A.E., and Yeh, P., *Image amplification by two-wave mixing in photorefractive crystals*. appl. Opt., 1990. **39**: p. 3026-9.

[Hong, '93]. Hong, J.H. and Chang, T.Y., *Frequency-agile rf notch filter that uses photorefractive two-beam coupling*. Opt. Lett., 1993. **18**: p. 164-6.

[Horowitz, '91a]. Horowitz, M. and Fischer, B., *Photorefractive novelty filters and the dynamics of their nonlinear wave mixing*. Proceedings of the 17th Convention of Electrical and Electronics Engineers in Israel, 1991a: p. xiv+429, 10-14.

[Horowitz, '91b]. Horowitz, M., Kligler, D., and Fischer, B., *Time-dependent behavior of photorefractive two- and four-wave mixing*. J. Opt. Soc. Am. B, 1991b. **8**(10): p. 2204-17.

[Ing, '91]. Ing, R.K. and Monchalin, P., *Broadband optical detection of ultrasound by two-wave mixing in a photorefractive crystal*. Appl. Phys. Lett., 1991. **59**: p. 3233-5.

[Jahoda, '84]. Jahoda, F.C., Weber, P.G., and Feinberg, J., *Optical feedback, wavelength response, and interference effects of self-pumped phase conjugation in $BaTiO_3$*. Opt. Lett., 1984. **9**(8): p. 362-4.

[Joseph, '92]. Joseph, J., *et al.*, *Real-time image processing using selective erasure in photorefractive two-wave mixing*. Appl. Opt., 1992. **31**: p. 4769-72.

[Jungner, '95]. Jungner, P., *et al.*, *Absolute frequency of the molecular Iodine transition R(56) 32-0 near 532nm*. IEEE Trans. Instrum. Meas., 1995. **44**: p. 151-4.

[Khoury, '91]. Khoury, J., Woods, C.L., and Cronin-Golomb, M., *Photorefractive holographic interference novelty filter*. Opt. Commun., 1991. **82**(5-6): p. 533-8.

[Khoury, '93]. Khoury, J., Ryan, V., and Cronin-Golomb, M., *Photorefractive frequency converter and phase-sensitive detector*. J. Opt. Soc. Am. B, 1993. **10**(1): p. 72-82.

[Khoury, '94]. Khoury, J., *et al.*, *All-optical joint Fourier transform correlator*. Appl. Opt., 1994. **33**: p. 8216-25.

[Klein, '86a]. Klein, M.B., *et al.*, *Imaging threshold detector using a phase-conjugate resonator in $BaTiO_3$*. Opt. Lett., 1986a. **11**(575-577).

[Klein, '86b]. Klein, M.B. and Valley, G.C., *Characteristics of $BaTiO_3$ for electro-optic devices.* Proc. SPIE - Int. Soc. Opt. Eng., 1986b. **567**: p. 116-20.

[Kogelnik, '69]. Kogelnik, H., *Coupled wave theory for thick hologram gratings*. Bell Syst. Tech. J., 1969. **48**(2909-2947).

[Kukhtarev, '79]. Kukhtarev, N.V., *et al.*, *Holographic storage in elctrooptic crystals. II. Beam coupling - Light amplification*. Ferroelectrics, 1979. **22**: p. 961-4.

[Kuwata-Gonokami, '95]. Kuwata-Gonokami, M., *et al.*, *Polymer microdisk and microring lasers*. Opt. Lett., 1995. **20**(20): p. 2093-5.

[LaGasse, '94]. LaGasse, M.J., *et al.*, *Optical carrier filtering for high dynamic range fibre optic links*. Electron. Lett., 1994. **30**(25): p. 2157-8.

[Lin, '98]. Lin, Y., *et al.*, *Observation of the disk mode pattern in organic microdisk*. Solid State Comm., 1998. **105**(7): p. 445-8.

[Lindsay, '70]. Lindsay, R.B., *Lord Rayleigh- the man and his work*. 1970, New York: Pergamon Press.

[Lininger, '90]. Lininger, D.M., *et al.*, *Theory of bistability and self pulsing in a ring resonator with saturable photorefractive gain and loss*. Opt. Commun., 1990. **76**: p. 89-96.

[Liu, '93]. Liu, L. and Liu, X., *Matrixing coupled wave theory of photorefractive hologram recorded by two-beam coupling*. J. Mod. Opt., 1993. **40**(11): p. 2257-65.

[Loayssa, '00]. Loayssa, A., Benito, D., and Garde, R.T., *Optical carrier-suppression technique with a Brillouin-erbium fiber laser*. Opt. Lett., 2000. **25**(4): p. 197-9.

[MacCormack, '96]. MacCormack, S. and Feinberg, J., *Revealing 180° domains in ferroelectric crystals by phorefractive beam coupling*. Appl. Opt., 1996. **35**(30): p. 5961-3.

[Marrakchi, '90]. Marrakchi, A., *et al.*, *Dynamic holographic interconnects with ananlog weights in photorefractive crystals*. Opt. Eng., 1990. **29**(3): p. 215-24.

[Mazur, '99]. Mazur, A., *et al.*, *Light-induced charge transport in photorefractive $BaTiO_3$:Fe and $Ba_{0.77}Ca_{0.23}TiO_3$:Fe*. Radiat. Eff. Defects Solids (Switzerland), 1999. **150**(1-4): p. 673-8.

[Mills, '85]. Mills, P. and Paige, E.G.S., *Holographically formed, highly selective, infra-red filter in iron-doped lithium niobate*. Electron. Lett., 1985. **21**: p. 885-6.

[Min, '88]. Min, K., *et al.*, *Automated two speaker separation system*. Intern. Conf. on Acoustics, Speech and Sig. Proc., 1988: p. 5 vol. 2928, 537-40 vol.1.

[Mok, '91]. Mok, F.H., Tackitt, M.C., and Stoll, H.M., *Storage of 500 high-resolution holograms in a $LiNbO_3$ crystal*. Opt. Lett., 1991. **16**(8): p. 605-7.

[Montgomery, '95]. Montgomery, R. and DeSalvo, R., *A novel technique for double sideband suppressed carrier modulation of optical fields*. IEEE Photon. Tech. Lett., 1995. **7**(4): p. 434-6.

[Murray, '00]. Murray, T.D., Tuovinen, H., and Krishnaswamy, S., *Adaptive optical array receivers for detection of surface acoustic waves*. Appl. Opt., 2000. **39**(19): p. 3276-84.

[Neifeld, '93]. Neifeld, M.A. and Psaltis, D., *Programmable image associative memory using an optical disk and a photorefractive crystal*. Appl. Opt., 1993. **32**(23): p. 4398-409.

[Psaltis, '88]. Psaltis, D., Brady, D., and Wagner, K., *Adaptive optical networks using photorefractive crystals*. Appl. Opt., 1988. **27**(1752-1759).

[Puoet, '96]. Puoet, B.F., *et al.*, *Heterodyne interferometer with two-wave mixing in photorefractive crystals for ultrasound detection on rough surfaces*. Appl. Phys. Lett., 1996. **69**: p. 3782-4.

[Rakuljic, '93]. Rakuljic, G.A. and Leyva, V., *Volume holographic narrow-band optical filter*. Opt. Lett., 1993. **18**(6): p. 459-61.

[Ringhofer, '00]. Ringhofer, K.H., *et al.*, *Shaping of photorefractive two-wave coupling by fast phase modulation*. Phys. Rev. E, 2000. **61**(2): p. 2029-37.

[Saffman, '91]. Saffman, M., Benkert, C., and Anderson, D.Z., *Self-organizing photorefractive frequency demultiplexer*. Opt. Lett., 1991. **16**: p. 1993-5.

[Saxena, '90]. Saxena, R., *et al.*, *Diffraction properties of multiple-beam photorefractive gratings*. J. Opt. Soc. Am. B, 1990. **7**(7): p. 1210-5.

[Sayano, '88]. Sayano, K., Rakuljic, G.A., and Yariv, A., *Thresholding semilinear phase conjugate mirror*. Opt. Lett., 1988. **13**: p. 143-5.

[Schiller, '91].Schiller, S. and Byer, R.L., *High-resolution spectroscopy of whispering gallery modes in large dielectric spheres*. Opt. Lett., 1991. **16**(15): p. 1138-40.

[Schiller, '92].Schiller, S., *et al.*, *Fused-silica monolithic total-internal-reflection resonator*. Opt. Lett., 1992. **17**(5): p. 378-80.

[Scruby, '90]. Scruby, C.B. and Drain, L.E., *Laser Ultrasonics, Techniques and Applications*. 1990, Bristol, UK: Adam Hilger.

[Sharp, '94]. Sharp, E.J., *et al.*, *Photorefractive image processing using mutually-pumped phase conjugators*. Proc. SPIE – Int. Soc. Opt. Eng., 1994. **2237**: p. 347-59.

[Solymar, '96]. Solymar, L., Webb, D.J., and Grunnet-Jepsen, A., *The physics and applications of photorefractive materials*. Oxford series in optical and imaging sciences II. 1996, New York: Oxford University Press Inc.

[Staebler, '75]. Staebler, D.L., *et al.*, *Multiple storage and erasure of fixed holograms in Fe-doped $LiNbO_3$*. Appl. Phys. Lett., 1975. **26**: p. 182-4.

[Stojkov, '92].Stojkov, P., Timotijevic, D., and Belic, M., *Symmetries of two-wave mixing in photorefractive crystals*. Opt. Lett., 1992. **17**(20): p. 1406-8.

[Tonda-Goldstein, '00]. Tonda-Goldstein, S., *et al.*, *Stimulated Brillouin scattering for microwave signal modulation depth increase in optical links*. Electron. Lett., 2000. **36**(11): p. 944-6.

[Uesu, '95]. Uesu, Y., *et al.*, *Recent development of optical novelty filter and dynamics of optical novelty filter with use of the CAT-type self-pumped phase conjugate mirror*. Ferroelectrics, 1995. **174**(1-2): p. 133-48.

[Volk, '94]. Volk, T., Rubinina, N., and Wohlecke, M., *Optical-damage-resistant impurities in lithium niobate*. J. Opt. Soc. Am. B, 1994. **11**(9): p. 1681-7.

[Weiss, '89]. Weiss, S., *et al.*, *Photorefractive dynamic optical interconnects*. Proc. SPIE - Int. Soc. Opt. Eng., 1989. **1018**: p. 55-7.

[White, '82]. White, J.O., *et al.*, *Coherent oscillation by self-induced gratings in the photorefractive crystal BaTiO3*. Appl. Phys. Lett., 1982. **40**: p. 450-2.

[Ye, '96]. Ye, J., *et al.*, *Hyperfine structure and absolute frequency of the* $^{87}Rb5P_{3/2}$ *state*. Opt. Lett., 1996. **21**(16): p. 1280-2.

[Yeh, '85]. Yeh, P., *Theory of Unidirectional Photorefractive Resonators*. J. Opt. Soc. Am. B, 1985. **2**: p. 1924-8.

[Yeh, '88]. Yeh, P., Chang, T.Y., and Ewbank, M.D., *Model for mutually pumped phase conjugation*. J. Opt. Soc. Am., 1988. **5**: p. 1743-9.

[Yeh, '92]. Yeh, P., *Photorefractive phase conjugators*. Proc. IEEE, 1992. **80**(3): p. 436-50.

[Yeh, '93]. Yeh, P., *Introduction to Photorefractive Nonlinear Optics*. 1993, New York: John Wiley & Sons Inc.

[Yu, '92]. Yu, F.T.S., *et al.*, *Optical novelty filter with phase carrier*. Opt. Commun., 1992. **92**(4-6): p. 205-8.

[Yu, '94]. Yu, F.T.S., Yin, S., and Wang, C.-M., *A content addressable polychromatic neural net using a (Ce:Fe)-doped* $LiNbO_3$ *photorefractive crystal*. Opt. Commun., 1994. **107**: p. 300-8.

[Zel'dovich, '95]. Zel'dovich, B.Y., Mamaev, A.V., and Shkunov, V.V., *Speckle-wave interactions in application to holography and nonlinear optics*. 1995, Boca Raton, FL: CRC Press, Inc.

[Zozulya, '95]. Zozulya, A. and Anderson, D.Z., *Spatial structure of light and nonlinear refractive index generated by fanning in photorefractive media*. Phys. Rev. A, 1995. **52**: p. 878-81.

[Zozulya, '95]. Zozulya, A.A., Saffman, M., and Anderson, D.Z., *Stability analysis of two photorefractive ring resonator circuits: the flip-flop and the feature extractor*. J. Opt. Soc. Am. B, 1995. **12**: p. 1036-47.